Atmos. Meas. Tech. Discuss., 6, 9397–9465, 2013
www.atmos-meas-tech-discuss.net/6/9397/2013/
doi:10.5194/amtd-6-9397-2013

Atmospheric Measurement Techniques Discussions

Performance of a geostationary mission, geoCARB, to measure CO_2, CH_4 and CO column-averaged concentrations

I. N. Polonsky[1], D.M. O'Brien[2], J. B. Kumer[3], C. W. O'Dell[4], and the geoCARB Team[5]

[1]Cooperative Institute for Research in the Atmosphere, Colorado State University, USA
[2]OBrien R&D LLC, Livermore, Colorado, USA
[3]Advanced Technology Center, Lockheed-Martin, Palo Alto, USA
[4]Department of Atmospheric Science, Colorado State University, USA
[5]University of Oklahoma, Norman, USA, and Advanced Technology Center, Lockheed-Martin, Palo Alto, USA

Received: 11 October 2013 – Accepted: 15 October 2013 – Published: 31 October 2013

Correspondence to: I. N. Polonsky (polonsky@atmos.colostate.edu)
and D. M. O'Brien (obrien@atmos.colostate.edu)

Published by Copernicus Publications on behalf of the European Geosciences Union.

Abstract

GeoCARB is a proposed instrument to measure column averaged concentrations of CO_2, CH_4 and CO from geostationary orbit using reflected sunlight in near-infrared absorption bands of the gases. The scanning options, spectral channels and noise characteristics of geoCARB and two descope options are described. The accuracy of concentrations from geoCARB data is investigated using end-to-end retrievals; spectra at the top of the atmosphere in the geoCARB bands are simulated with realistic trace gas profiles, meteorology, aerosol, cloud and surface properties, and then the concentrations of CO_2, CH_4 and CO are estimated from the spectra after addition of noise characteristic of geoCARB. The sensitivity of the algorithm to aerosol, the prior distributions assumed for the gases and the meteorology are investigated. The contiguous spatial sampling and fine temporal resolution that geoCARB could provide opens the possibility of monitoring localised sources such as power plants. Simulations of emissions from a power plant with a gaussian plume are conducted to assess the accuracy with which the emission strength may be recovered from geoCARB spectra. Scenarios for "clean" and "dirty" power plants are examined. It is found that a reliable estimate of the emission rate is possible, especially for power plants that have particulate filters, by averaging multiple snap-shots of the CO_2 field surrounding the plant. The result holds even in the presence of partial cloud cover.

1 Introduction

The Greenhouse gases Observing SATellite (GOSAT) launched in 2009 by the Aerospace Exploration Agency (JAXA) of Japan and NASA's forthcoming Orbiting Carbon Observatory (OCO-2) are exploratory missions to measure concentrations of CO_2 and CH_4 (GOSAT only) from spectra of reflected sunlight with sufficient accuracy to determine sources and sinks of these greenhouse gases on regional scales (hundreds of kilometres). While the results from GOSAT are being refined rapidly and OCO-2 pro-

AMTD
6, 9397–9465, 2013

gresses towards launch in July 2014, planning has begun for missions that will have the additional capability to target both point and diffuse sources and sinks on smaller scales (tens of kilometres). The key to such missions is to make a dense set of observations of the target area. For example, the CarbonSat concept (Bovensmann et al., 2010a) has characteristics similar to OCO-2, but proposes a 500 km swath with 2 km footprints. Comprehensive studies by Bovensmann et al. (2010b) and Velazco et al. (2011) have estimated the accuracy with which emissions from coal-fired power plants might be measured by CarbonSat or a constellation of CarbonSats. The studies include instantaneous emissions as well as monthly and annual averages of emissions. Overflights with an airborne CH_4 and CO_2 sensor (MAMAP) lend strong support to CarbonSat (Gerilowski et al., 2011; Krings et al., 2011).

Another proposed instrument is geoCARB, whose goal is to advance scientific understanding of human impacts on the global carbon cycle, and to demonstrate a greenhouse gas source monitoring technique that could support national goals or international agreements on greenhouse gas emission reductions. The baseline mission for geoCARB aims to produce column-averaged mixing ratios of CO_2, CH_4 and CO with accuracy per sample of 0.7 % (≈ 2.7 ppm), 1 % (≈ 18 ppb) and 10 % (≈ 10 ppb) respectively at continental scales with contiguous spatial sampling of a few kilometres, multiple times each day. The threshold mission sacrifices CO while retaining the baseline targets for CO_2 and CH_4.

GeoCARB proposes to place grating spectrometers in geostationary orbit to measure spectra of reflected sunlight in the O_2 A-band at 0.76 µm, the weak and strong CO_2 bands at approximately 1.61 µm and 2.06 µm and the bands of CH_4 and CO near 2.33 µm. Geostationary orbit (GEO) offers several advantages over low-earth orbit (LEO). Firstly, GEO allows longer observations, thereby enabling higher signal-to-noise ratio (SNR), because SNR is proportional to the square root of the dwell time for detectors limited by photon shot noise. Secondly, areas with high and uncertain anthropogenic emissions of CO_2, CH_4 and CO may be targetted with contiguous sampling, relatively small spatial footprints and fine temporal resolution. Several observations

AMTD
6, 9397–9465, 2013

per day on continental scales are possible. Of course, GEO also poses challenges. For a given size footprint, pointing and after-the-fact geolocation are more difficult than from LEO. Nevertheless both are manageable using data from a star tracker and landmarks on the surface of the earth. This remains true even if geoCARB is deployed as a hosted payload on a geostationary commercial communications satellite, for which pointing requirements usually are less stringent. In addition, spatial resolution is smeared, and the deleterious effects of aerosols and clouds are problematic for observations far from the sub-satellite point (SSP). The latter may be mitigated partially because the longer viewing path through the atmosphere enhances the absorption in molecular features. On balance, the possibility of a relatively inexpensive deployment of geoCARB as a hosted payload coupled with the advantages of GEO mean that the concept warrants close investigation.

This paper outlines the geoCARB instrument, estimates the accuracy with which geoCARB might estimate column-averaged concentrations of CO_2, CH_4 and CO, and presents initial simulations for power plant emissions as seen by geoCARB. In addition to the baseline instrument proposed for geoCARB, the paper also examines two options for descoping the mission. The study is guided by the excellent work that has been done for OCO-2 and GOSAT, and draws heavily on the papers published by O'Dell et al. (2012) and Crisp et al. (2012). Further details of geoCARB may be found in the papers by Kumer et al. (2013b), Sawyer et al. (2013) and Mobilia et al. (2013).

The paper begins with an overview of geoCARB, specifying the baseline instrument characteristics and the descope options. Next follows a summary of the methods and data used to simulate geoCARB spectra and to retrieve the trace gas concentrations from the spectra. This section is relatively brief because the procedures are by now familiar and well documented (O'Dell et al., 2012, for example). Subsequent sections cover the accuracy of retrieved column-averaged dry-air mole fractions of CO_2, CH_4 and CO, respectively denoted X_{CO_2}, X_{CH_4} and X_{CO}.

AMTD
6, 9397–9465, 2013

2 GeoCARB

While geoCARB would provide important new insights into the carbon cycle whatever the longitude of its deployment, for definiteness we will assume a nominal longitude of 110° E (±10°), from which geoCARB would observe a significant part of the Asian-Pacific region. Its mapping capability would enable geoCARB to observe changes in urban and industrial emissions over Asia, and to capture variations in flux consistent with key natural drivers. This area has the largest current anthropogenic CO_2 emissions, and it is where the perturbation is growing fastest and uncertainties are the largest. China is the world's largest emitter of anthropogenic CO_2 and CH_4, and India is currently the third largest emitter of anthropogenic CO_2 and second largest for CH_4. In 2008, China, India and Indonesia contributed more than 30 % of the global flux of anthropogenic CH_4. By 2008, China was emitting twice as much CO as the USA, and India had already passed the USA in CO emissions. Since 2003, CO_2 emission from China has more than doubled, while from India it has increased by 60 % (EDGAR, 2011; VULCAN, 2011). Australia, while not a major emitter, would provide easily accessible instrumented targets in geoCARB's field of view for calibration and validation.

To achieve the sampling and accuracy required to determine column-integrated CO_2, CH_4 and CO from GEO, geoCARB proposes to use a near infra-red (NIR) slit imaging spectrometer that measures reflected sunlight in absorption bands of these gases. An additional channel, measuring the O_2 column concentration, is required to derive the column average mixing ratios at high precision (Crisp et al., 2004). By scanning the north-south slit across the Earth, this instrument provides observations that are unique: continental-scale coverage with high spatial and temporal resolution.

2.1 Scanning

Figure 1 illustrates potential scan blocks to view the important source regions from 110° E. The spectra necessary to retrieve the CO_2, CH_4 and CO columns are acquired with two-times oversampling of the native east-west resolution of the instru-

AMTD
6, 9397–9465, 2013

ment, which is approximately 3 km at the sub-satellite point (SSP). The north-south extent of any scan block is fixed, with 1016 samples over a 4.4° field of view, corresponding to 25° in latitude or 2800 km at the SSP. An integration time of 4.08 s and a total time per step of 4.42 s yield the scan times shown in Fig. 1 and complete coverage in less than eight hours. By exploiting the diurnal patterns of solar illumination, the entire region typically can be scanned at least twice per day (depending on the season).

The geoCARB scan patterns are flexible and the scan strategy can be updated to observe targets of interest or transient events. The central latitude can be programmed to vary over the course of a scan, and specific regions can be scanned multiple times in one day in a dedicated target mode.

With this approach to regional monitoring of CO_2, geoCARB is highly complementary to OCO-2. Figure 2 illustrates the differences between the geoCARB and OCO-2 scanning geometries. Whereas OCO-2 provides measurements over the entire Earth, its ground track repeat cycle is sixteen days and it crosses the target region in Fig. 2 only twice eight days apart. In contrast, geoCARB can scan the region shown in Fig. 2 in less than six minutes, so an hour of dedicated observation on a clear day could provide ten snap-shots, sufficient to estimate current emissions from the power plants (Bovensmann et al., 2010b).

2.2 Spectrometer

GeoCARB employs a steerable mirror system, directing Earth-reflected light into two grating spectrometers, each with two channels. One spectrometer (SW) covers the O_2 A-band at 0.763 µm and the 1.611 µm CO_2 band; the second spectrometer (LW) captures the strong CO_2 band at 2.065 µm and the CO and CH_4 bands near 2.323 µm. Both spectrometers are cooled to 125 K, principally to minimise the thermal background in the 2.065 µm and 2.323 µm bands. Each spectrometer has just one grating, used in different orders for the two bands, which are separated by order sorting filters. Each band has its own focal-plane array (FPA), so there are four FPAs for the baseline in-

AMTD
6, 9397–9465, 2013

strument. The Earth is observed through a slit aligned north-south; the grating spreads the wavelengths in the orthogonal direction.

Two descope options are investigated. In the first, the SW spectrometer is retained in the baseline configuration with two bands at 0.763 µm and 1.611 µm, while the LW spectrometer is shifted to capture the CH_4 band at approximately 1.662 µm. In the second descope option, the SW spectrometer loses the CO_2 band and keeps only the 0.763 µm O_2 A-band, but the LW spectrometer now spans bands of both CO_2 and CH_4 from 1599.5 nm to 1672.5 nm, capturing both on the same FPA. This configuration has lower spectral resolution than descope 1, but offers higher SNR. The bands and their spectral resolutions for the baseline and descope options are listed in Table 1.

The descope options lose the CO band and the strong CO_2 band, the former being more important because CO helps identify sources of CO_2. In compensation, the spectrometers may be operated at higher temperatures, and FPAs with associated optics are eliminated, one for descope 1 and two for descope 2. Thus, the cost savings are considerable, particularly for descope 2. The impact of the descope options on the accuracy with which X_{CO_2} and X_{CH_4} can be estimated will be examined in Sect. 5.

The optical design (Fig. 3) features an off-axis parabolic afocal telescope with a 72 mm entrance aperture and 4.4° field of view. With an entrance pupil at the primary mirror, the telescope produces collimated light for the system stop and a long-wavelength/short-wavelength beamsplitter. For each (LW and SW) leg, an f/3.2 objective lens group forms a well-corrected image on an 18 mm × 36 µm slit. The Littrow images are relayed to the focal planes by refractive relay lenses that correct aberrations and provide space to split the two bands to their respective focal planes. Order-selecting narrow band filters pass only the bands of interest to the respective FPAs. Due to fundamental optics constraints on the design, the spectrum from a given spatial pixel falls along a curve across the focal plane. To maintain a constant bandwidth, 780 spectral pixels are selected from the 1016 pixels in the focal plane. Each spatial point will use a different set of 780 spectral pixels, centered on the middle of the band for that spatial point.

AMTD
6, 9397–9465, 2013

2.3 Signal-to-noise ratio (SNR)

The noise model for geoCARB is based on both laboratory characterisation and airborne trials with the Tropospheric Mapping Imaging Spectrometer (TIMS) developed by Lockheed Martin (Kumer et al., 2009, 2011). TIMS was used to demonstrate the feasibility of measuring CH_4 and CO in the 2.33 µm band. Details of the noise model and further information on the detector performance are provided by Kumer et al. (2013a).

The noise equivalent spectral radiance N (in units $\mathrm{nW\,(cm^2\,sr\,cm^{-1})^{-1}}$) for a representative spectral sample consists of shot noise due to the observed signal radiance I and a signal independent noise floor radiance N_0. It is given by

$$N = \sqrt{N_0^2 + N_1 I},$$

where N_0 and N_1 are constants for each band[1]. Their numeric values, listed in Table 2, were derived from geoCARB instrumental and operational parameters by Kumer et al. (2013a)[2].

For convenience, the noise is estimated in terms of the radiance I reflected in a transparent atmosphere from a surface with albedo A,

$$I = FA\cos\theta_s/\pi,$$

where F is the solar flux density at the top of the atmosphere and θ_s is the solar zenith angle. The SNR may be expressed in terms of the product $A\cos\theta_s$,

$$\mathrm{SNR} = I/N = (FA\cos\theta_s/\pi)/\sqrt{N_0^2 + N_1(FA\cos\theta_s/\pi)},$$

[1] In practice N_0 and N_1 will vary from pixel to pixel, and their values will be determined by careful pre-flight calibration. However, in this paper we use average values for each band.

[2] The parameters in Table 2 differ slightly from those given by Kumer et al. (2013a) because the latter were revised after the lengthy simulations for this paper had commenced. However, the differences are small, and they have negligible impact on the results.

AMTD
6, 9397–9465, 2013

which is used to predict the signal-to-noise ratios in Fig. 4. Table 3 lists values of $A\cos\theta_s$ such that

$$N_0^2 = N_1 I,$$

demonstrating that shot noise dominates even for very weak illumination.

3 Simulated spectra

In order to generate an ensemble of spectra with which to test the retrieval algorithm, the OCO simulator (O'Brien et al., 2009) was modified to have the channels, spectral resolution and noise model of geoCARB, but the sun-synchronous orbit of OCO was retained. By flying multiple orbits, wide ranges of cloud, aerosol, surface type, trace gas concentrations and solar zenith angle were encountered, thereby providing a comprehensive ensemble of spectra. Most of the results of this paper are based on these simulations along ten sun-synchronous orbits shown in Fig. 5. However, in the studies of emissions from power plants, the true orbit and scan geometry of geoCARB were modelled for specific targets.

To avoid circular results, the simulator forward model is more general and accurate than that used in the retrieval. It has higher vertical resolution, includes more types of clouds and aerosols, more complicated surface optical properties, and has more accurate radiative transfer. However, the simulations assume the same spectroscopy and instrument properties as in the retrieval.

3.1 Meteorology

Surface pressure and profiles of temperature and water vapour were derived from global forecasts from the European Centre for Medium-Range Weather Forecasts (ECMWF), as was the surface wind speed. The three-hourly forecasts were interpolated to the times and locations of the geoCARB observations. The interpolation

AMTD
6, 9397–9465, 2013

included an adjustment of surface pressure for the height of each observation point compared to the heights of its surrounding grid points.

3.2 Aerosol and cloud

Vertical distributions of aerosol and cloud in the simulated atmospheres were derived from CALIPSO (version 3). For each month and year of CALIPSO observations, measured profiles of aerosol and cloud within $2^\circ \times 2^\circ$ latitude and longitude boxes over the globe were compiled. For any geoCARB target, cloud and aerosol profiles were selected randomly from the compilation for the box containing the target, and those profiles then were used in the simulation of spectra at the top of the atmosphere in the geoCARB bands. The selected profiles may contain several types of aerosol and cloud, the number and types varying from sample to sample. No attempt was made to impose spatial correlation on the aerosol and cloud fields, because it was thought that maximizing the variability of cloud and aerosol, while still maintaining a link to reality through CALIPSO, would make the tests of the retrieval algorithm more stringent. In fact, over the dense grid of samples that geoCARB will acquire in flight, it is highly likely that aerosol and cloud will be correlated spatially, perhaps for many tens of kilometres. Such correlations should assist in correcting for aerosol and cloud when estimating the trace gas concentrations. Nevertheless, no assumption of uniformity of aerosol or cloud between pixels was made in the results reported here.

Each type of aerosol reported by CALIPSO was associated with a specific instance from AERONET observations (Dubovik et al., 2002) using the correspondence defined by O'Brien et al. (2009). For water clouds, the effective radius was drawn randomly from the global distribution derived from one year of MODIS by Polonsky (unpublished), and the optical properties were computed at the geoCARB bands from the optical thickness, layer-by-layer, reported by CALIPSO at 532 nm. Bimodal distributions for ice cloud particles were assumed, with effective radii depending on temperature as described by Ivanova et al. (2001). For each effective radius, the extinction coefficient, extinction efficiency and phase matrices were taken from Baum et al. (2005a, b).

AMTD
6, 9397–9465, 2013

3.3 Trace gas profiles

The vertical profiles of CO_2 in the simulator were derived from the Parameterised Chemical Transport Model (PCTM) (Kawa et al., 2004). For CO, the background profiles were drawn from MOPITT (Deeter et al., 2003, 2007a, b), with the global distribution of X_{CO} shown in Fig. 6. Profiles of CH_4 were taken from a snap-shot of the global CH_4 distribution calculated with the TM5 chemical transport model (Krol et al., 2005). In each case, the profiles were interpolated to the times and locations of the geoCARB observations.

3.4 Surface properties

Only land targets were analysed, because the ocean generally is too dark in the NIR when viewed from GEO[3]. The bidirectional reflectance distribution function (BRDF) of land targets was computed in two steps. First, a scalar BRDF was estimated from the MODIS sixteen-day BRDF product MCD43B1. This product contains coefficients for three kernels, the first representing isotropic reflection and the other two linearized approximations to the Li-sparse and Ross-thick kernels (Wanner et al., 1997; Li and Strahler, 1992). These coefficients, provided for each of seven MODIS channels, were interpolated to the end-points of the geoCARB bands. However, this purely scalar BRDF provides no information on the surface polarisation characteristics. The latter were estimated using a simple model based on POLDER observations (F.-M. Breon, personal communication, 2008), which were aggregated into a polarised BRDF model for each of the sixteen IGBP land surface types. This model, derived specifically for the POLDER 550 nm wavelength, was used directly; no wavelength interpolation was performed, so the polarisation characteristics are independent of wavelength. Thus, in the 4×4 polarised BRDF that describes how each Stokes parameter is reflected by

[3]This is not strictly true, because glint conditions can occur near the equator. Future work will include glint observations.

AMTD
6, 9397–9465, 2013

the surface into the four possible Stokes parameters, the $I \rightarrow I$ pathway was taken from the wavelength-dependent MODIS (MCD43B1) three-kernel model, and the remaining fifteen components were taken from the wavelength-independent POLDER model. While this model no doubt has flaws, it nonetheless should provide reasonably realistic surface BRDFs.

3.5 Radiative transfer and spectroscopy

Monochromatic radiance spectra were computed at the top of the atmosphere using the radiative transfer code described by Heidinger et al. (2006) and O'Dell et al. (2006). The technique of "low streams interpolation" (O'Dell, 2010) was used to reduce the computation time without sacrificing accuracy at a level well below the instrument noise. The spectroscopy was based on HITRAN 2004 (Rothman et al., 2009) plus CO_2 line updates from 4300–7000 cm^{-1} from Toth et al. (2008).

3.6 Instrument line shape function and spectral sampling

For each band, the instrument line shape function $L(\nu, \nu_0)$ was assumed to be gaussian,

$$L(\nu, \nu_0) = \frac{1}{\sqrt{2\pi}\sigma} \exp\left(-\frac{1}{2}(\nu - \nu_0)^2/\sigma^2\right), \quad (1)$$

where

$$\sigma = \frac{\Delta\nu}{2\sqrt{2\ln 2}} \quad (2)$$

and $\Delta\nu$ is the full width at half maximum. The relation between $\Delta\lambda$ in Table 1 and $\Delta\nu$ was taken to be

$$\Delta\nu = \frac{10^7 \Delta\lambda}{\lambda_{\min}\lambda_{\max}}, \quad (3)$$

AMTD
6, 9397–9465, 2013

where λ_{min} and λ_{max} are the band limits (in nm) from Table 1.

The spectral sampling was assumed to be uniform in the frequency domain,

$$\nu_k = \nu_1 + (k-1)\delta\nu, \quad (4)$$

where $k = 1, 2, \ldots, N_b$. The parameters for the geoCARB bands are listed in Table 4 for the baseline and descope options.

3.7 Noise

After calibration and correction for dark current, the detectors were assumed to be linear and to be free of zero-level offset. Noise computed as described in Sect. 2.3 was added to the spectra in all experiments. However, experience with GOSAT and OCO has shown that random noise from the instrument usually averages out in ensembles of retrievals, and that the persistent sources of error often lie elsewhere, such as in discrepancies between optical properties assumed within the retrieval algorithm and those occuring in the real (simulated) atmosphere. Consequently, experiments without instrument noise often are easier to interpret, and the conclusions usually remain valid when random noise is added.

4 Retrieval algorithm

4.1 Optimal estimation of profiles of trace gases

Optimal estimation as described by Rodgers (2000) was used to match modelled and observed spectra, using techniques similar to the algorithms developed for GOSAT and OCO but adapted to the bands and properties of geoCARB. Thus, a forward model simulated spectra at the top of the atmosphere using parameters from a state vector that characterised the atmosphere, surface and instrument. The parameters of the state vector were adjusted iteratively to minimise a cost function that balanced the differences between model and observations on one hand and the state and its prior on

AMTD
6, 9397–9465, 2013

the other. Prior estimates and covariances for the parameters in common with GOSAT were the same as those used by O'Dell et al. (2012).

The forward model accounted for multiple scattering caused by molecules, aerosols and clouds. It computed Stokes vector at the top of the atmosphere, which then was combined with the polarisation Mueller matrices for the spectrometers to predict the measured spectra. For the results in this paper, it was assumed that polarisation scramblers were in place, so that only Stokes intensity was measured. Later studies will incorporate the predicted polarisation sensitivity of the geoCARB spectrometers.

When comparing CO_2 profiles with the truth, the averaging kernel was taken into account in the way described by Connor et al. (2008). Thus, if X_r is the retrieved X_{CO_2}, whose true vertical profile is $\boldsymbol{x}_m$, we compared X_r with X_m defined by

$$X_m = X_a + \boldsymbol{h}^* \mathbf{A}(\boldsymbol{x}_m - \boldsymbol{x}_a),$$

where $\boldsymbol{x}_a$ is the prior profile of CO_2 assumed in the retrieval, X_a is the corresponding prior estimate of X_{CO_2}, $\mathbf{A}$ is the matrix of the CO_2 elements of the averaging kernel, and $\boldsymbol{h}$ is the pressure weighting function containing the layer-by-layer profile of the molar mass of dry air normalised by the molar mass of dry air in the total column.

In the baseline configuration, full vertical profiles of CO_2 and H_2O and scaling factors for the prior profiles of CH_4 and CO were estimated simultaneously from spectra in all four bands using the standard formalism (Rodgers, 2000). The state vector included both vertical profiles (CO_2, H_2O, two types of aerosol, one type of ice cloud and one type of water cloud) and scaling factors (CH_4 and CO). The aerosol types were Kahn types 2b and 3b (Kahn et al., 2001); the cloud types were selected by assigning the effective radius, usually 70 µm for ice and 8 µm for water. The vertical distributions of aerosol and clouds used parameterised profiles. The temperature profile was held at the prior profile from ECMWF meteorology, apart from an offset that was adjusted. Surface parameters included the pressure and a model linear in wavelength for the Lambertian albedo within each band. Spectral offsets were included to allow for the

AMTD
6, 9397–9465, 2013

combination of instrument drift and Doppler shifts, although the latter should be known with high accuracy in practice.

Because the CO_2 bands do not overlap those of CH_4 and CO in the 2.323 µm region of the baseline configuration, it would have been possible to break the retrieval into two parts, the first retrieving CO_2 and H_2O from the O_2 A-band, weak CO_2 band and strong CO_2 band, and the second retrieving CH_4, CO and H_2O from the O_2 A-band and the 2.323 µm band. However, that approach could lead to inconsistent profiles for H_2O and aerosol in the separate retrievals. Therefore, we preferred to perform a simultaneous retrieval with all four bands in order to ensure consistency of the H_2O and aerosol profiles.

A similar approach using all available bands simultaneously was used for the descope options, except that CO was not estimated.

4.2 Cloud screening

Because photons scattered by cloud and aerosol can either shorten or lengthen the mean photon path, reliable screening for cloud and aerosol is essential if column concentrations are to be inferred accurately from spectra of reflected sunlight. For GOSAT and OCO-2, the screening for cloud is applied as a pre-filter to avoid costly processing of cloud contaminated spectra. Typically, two screening methods are used.

The first is the O_2 A-band screening for cloud described by Taylor et al. (2012). In simplified terms, the screening algorithm performs a single iteration inversion in the O_2 A-band to estimate surface pressure and surface albedo, assuming that the sky is free of cloud and aerosol. If the estimated surface pressure differs significantly from the surface pressure from the ECMWF forecast, then the scene is diagnosed as cloudy and discarded. In practice, several minor refinements are needed, such as checking that the residual χ^2 is sufficiently small and that the estimated surface albedo is close to the value expected from MODIS observations.

The second, devised by Frankenberg at JPL, uses IMAP-DOAS (Frankenberg et al., 2005) in each of the CO_2 bands to estimate the column concentration of CO_2. If the

AMTD
6, 9397–9465, 2013

sky is free of cloud and aerosol, then the two answers should be the same, barring biases arising from errors in spectroscopy. Therefore, the algorithm in its simplest form computes the ratio of the two concentrations, and then rejects scenes when the ratio departs significantly from unity.

In the simulations for this paper, where computational efficiency was not a major issue, a pre-filter for cloud was not used, and all spectra were submitted to the retrieval algorithm. Cloudy scenes generally lead to large residual χ^2, and the estimated AOD generally exceeds the threshold set in the post-processing filter described below. Nevertheless, some cloudy scenes slipped through the post-processing filter, so the results presented here are pessimistic, though only slightly so. Prior screening for cloud based on the measured (or simulated) spectra will be implemented in later work.

4.3 Post-processing filters

A post-processing filter (PPF) is needed to reject cases where the model approximation to the spectra is poor. This may happen for many reasons, but the majority of cases occur when the optical properties assumed for aerosol and cloud do not match those used to simulate the spectra. Because this misrepresentation usually will manifest itself in high values of the reduced χ^2, a post-processing filter typically will reject cases where χ^2 exceeds a preset threshold. Other tests include checking the sizes of the posterior estimates of errors in the retrieved parameters, the number of degrees of freedom for signal, and the total aerosol optical depth.

Only a simple, generic filter was used for this study. Firstly, it checked only the χ^2 in the bands used to retrieve CO_2, because aerosol contamination, the most common cause of poor spectral fits, generally will affect all spectral bands similarly. Secondly, the filters were not optimised for specific regions, seasons or observation geometries; instead, the thresholds were the same for all cases. For the baseline configuration, the filter checked χ^2, the retrieved aerosol optical depth at the blue end of the O_2 A-band and the number of degrees of freedom for signal in the retrieved profile of CO_2. For the descope options, where the strong CO_2 band was sacrificed, the number of degrees

AMTD
6, 9397–9465, 2013

of freedom for CO_2 was smaller (typically near one), and a more effective filter was found to be the size of the posterior estimate for the error in retrieved X_{CO_2}. The filter is summarised in Table 5.

The tests included in the post-processing filter can take many forms and can be numerous, as has been found with GOSAT. Indeed, the post-processing filter for GOSAT has evolved in parallel with refinements to the retrieval algorithm. It is highly likely that the same will occur for geoCARB.

A subtle, but important, point concerning instrument noise will arise if geoCARB flies. When dealing with real observations, there will be persistent differences between modelled and measured spectra, some arising from errors in the spectroscopy data base, and others from mis-characterisation of the spectrograph. For GOSAT, and also for OCO-2 in the future, these systematic residuals are combined with the true instrument noise to produce an "empirical noise" that is used in the cost function when fitting the model to the data. The optimization stops when the residuals are comparable with the empirical noise, and in that case χ^2 is close to unity. If the instrument noise alone were used in the cost function, then the residuals never would be brought to the noise level, thanks to the persistent spectral artifacts, and χ^2 would exceed the ideal value of unity. Thus, careful accounting of persistent spectral biases will be needed to devise robust PPFs that test the χ^2 of the fits. Of course, for the simulated spectra in this paper, the same spectroscopy is used in the forward and retrieval algorithms and the spectrograph is assumed to be perfectly characterised, so the concept of empirical noise is not needed.

AMTD
6, 9397–9465, 2013

5 Analysis

5.1 Feasibility of descoping the strong CO_2 band

5.1.1 Tests with simulated spectra

The strong CO_2 band at 2.065 µm and the CH_4 and CO band at 2.323 µm require the LW spectrograph to be cooled to 125 K. If it could be shown that the strong CO_2 band is not essential, and if CH_4 could be retrieved from the band near 1.67 µm, then the geoCARB spectrograph could be simplified and reduced in cost. The penalty would be the loss of the CO channel. As a preliminary step in evaluating this descope option, a similar descope for GOSAT was considered in which retrievals of X_{CO_2} were performed without the strong CO_2 band.

The methodology for this test was as follows.

1. The GOSAT simulator was used to generate radiance spectra at the top of the atmosphere with realistic representations of both atmosphere and surface.

2. The GOSAT retrieval algorithm was used to analyse the radiance spectra assuming different levels of noise in the strong CO_2 band. The noise was amplified by factors of $1, 2, 4, 10^3, 10^6$ and 10^8. As the noise is increased, the importance of the strong CO_2 spectrum in the retrieval declines. By the time the multiplier has reached 10^3, the strong CO_2 spectrum plays no significant role, thereby imitating the situation where the strong CO_2 channel has been descoped.

3. A post-processing filter was applied to the output from the retrieval algorithm to eliminate poor fits to the spectra.

Figure 7 shows the signal-to-noise ratio currently used in the instrument model of the GOSAT simulator for the strong CO_2 band. Also shown is the product of the surface albedo and cosine of the solar zenith angle. The system is almost shot noise limited,

AMTD
6, 9397–9465, 2013

which explains the approximately square root dependence of the SNR upon the radiance. It is clear from this plot that increasing the noise by a factor of 10^3 or larger effectively eliminates the strong CO_2 band from the retrieval process.

Histograms of the error in retrieved X_{CO_2} for different scaling factors (1, 2, 4, 1000) of the noise in the strong CO_2 band are shown in Fig. 8. Each histogram shows the bias (mean), the standard deviation and the number of soundings that passed the post-processing filter. The panels on the left show the X_{CO_2} biases, while those on the right apply to surface pressure. Only cases that passed the post-processing filter are included in the histograms. With increasing noise level in the strong CO_2 band:

1. the mean error of the X_{CO_2} retrieval shifts gradually from 0.4 ppm to −1.15 ppm;
2. the standard deviation of the error in the retrieved X_{CO_2} remains practically unchanged;
3. the means and standard deviations of the surface pressure histograms vary little;
4. the number of soundings passing the post-processing filter is roughly constant.

In nearly all retrievals of X_{CO_2} from GOSAT spectra, it has been observed that the error in X_{CO_2} is negatively correlated with the error in surface pressure. The same is observed in this experiment (Fig. 9). However, as the importance of the strong CO_2 band is reduced with increasing noise level, the strength of the correlation weakens. For the nominal GOSAT instrument with scaling factor of unity, the correlation coefficient is −0.66, but decreases to −0.18 by the time the scaling factor has reached 1000. It is not obvious why this occurs, but it does suggest a coupling between the strong CO_2 band and the O_2 A-band that does not exist for the weak CO_2 band. Perhaps it is related to the strength of the bands, in that both the strong CO_2 band and the O_2 A-band have very strongly absorbing lines that sample the upper regions of the atmosphere.

AMTD
6, 9397–9465, 2013

5.1.2 Tests with TCCON spectra

Following on from Sect. 5.1.1, data from GOSAT and from the Lamont site of the Total Carbon Column Observation Network (TCCON) were compared to see if the features observed with simulated spectra persist in real spectra. The methodology was similar.

1. GOSAT observations for the years 2009–2011 (versions v050050 to v110110) falling within a distance of 500 km of Lamont were extracted, retrievals were performed, and then the post-processing filters described by Crisp et al. (2012) were applied to select soundings whose accuracy is expected to be high.

2. Corresponding TCCON observations with a ±30 min time window were used as truth.

3. The retrievals of X_{CO_2} were repeated with multiplicative factors of 1, 2, 4, 10 and 100 applied to the noise in the strong CO_2 band in order to reduce the impact of spectra in that band to effectively zero.

The comparison is shown in the panels of Fig. 10 for the five different scaling factors applied to the noise in the strong CO_2 band. Despite the increasing noise level, X_{CO_2} retrieved from GOSAT reproduces the annual cycle and trend quite well, apart from an increasing negative bias. This result is consistent with the findings from simulated spectra.

Again in parallel with the results from the simulated spectra, the bias in the retrieved surface pressure decreases steadily as the noise in the strong CO_2 band is amplified and the importance of that band to the retrieval decreases. However, the standard deviation of the error in the surface pressure remains almost unchanged. These results are shown in Table 6 and Fig. 11.

Finally, Table 6 and Fig. 12 present the mean and standard deviation of the error in retrieved X_{CO_2} as a function of the amplification of the noise in the strong CO_2 band. The correlation between X_{CO_2} retrieved from GOSAT and the values measured by TCCON remains strong for all levels of noise in the strong CO_2 band, and the slopes of

AMTD
6, 9397–9465, 2013

the correlations vary little. However, with increasing noise, the negative bias increases in magnitude, as noticed in the analysis with simulated spectra. The standard deviation of the biases increases slightly with the noise level, but the level is still smaller than that expected of the retrieval algorithm when analysing global GOSAT data (≈ 1.5 ppm).

The conclusions from this comparison between X_{CO_2} from TCCON and X_{CO_2} retrieved from GOSAT with increasing noise level in the strong CO_2 band are very similar to those from the study using simulated spectra. Amplifying the noise causes an increasingly negative bias in X_{CO_2} and a reduction in the surface pressure bias.

5.1.3 Implications for geoCARB

On the immediate evidence presented above, it is difficult to give a definitive answer as to whether or not it is safe to eliminate the strong CO_2 band. On the negative side, it causes the bias in retrieved X_{CO_2} to shift, an effect that has yet to be explained or understood. Furthermore, the strong CO_2 band has been found to help in both identifying scenes contaminated by cloud or aerosol and post-processing to eliminate poor fits to the spectra. On the positive side, eliminating the strong CO_2 band does not increase the standard deviation of the error in retrieved X_{CO_2}, and the correlation between biases in X_{CO_2} and surface pressure is weakened.

However, there are several other relevant factors.

1. The retrievals described above for GOSAT used an early version of the algorithm that contained almost unconstrained vertical profiles for four types of aerosol, giving a total of eighty aerosol parameters in the state vector. Subsequent research suggests that it is better to constrain the aerosol profiles so that each is represented by just a few parameters. Typically there are three, the height of the aerosol maximum, the width of its vertical distribution and the total aerosol optical depth. Thus, for four aerosol types, there are just twelve parameters. This refinement generally has reduced the size of the bias, bringing it into the range acceptable for geoCARB.

AMTD
6, 9397–9465, 2013

2. The initial guess for aerosol optical depth also is important. For the retrievals presented above it was set to 0.15, but recent evidence indicates that starting at 0.05 produces a smaller bias, particularly when used in conjunction with a tighter post-processing filter that selects soundings with less aerosol.

3. While bias in retrieved X_{CO_2} is critical if sources and sinks of CO_2 are to be estimated globally, it is less so for regional sources and sinks, especially when the surroundings of the source are sampled contiguously. For example, the plume of a power plant should stand out against the background, and even if the plume and the backgorund are negatively biased because the strong CO_2 band is not used, the difference between them still should be accurate. It is from the difference that the rate of emission is estimated. A similar argument should apply to emissions from small cities and to regional sinks.

4. Since these tests were performed, upgrades to solar spectrum and spectroscopy have reduced the mismatch between TCCON and GOSAT by a small but significant amount.

In summary, dependening on the balance between the objectives of geoCARB to study large (country-sized) and small (city-sized) sources and sinks, it appears feasible to relax the SNR requirement on the strong CO_2 band or to eliminate the band entirely. Both the descope options take the latter approach, and the simulations presented later show that the X_{CO_2} bias is modest and meets the mission requirements for geoCARB.

5.2 Experiment 1 – geoCARB retrievals with perfect meteorology and perfect trace gas priors

In the first experiment, the prior profiles for the trace gases (CO_2, CH_4 and CO) were equal to the truth, as also were the surface pressure and the profiles of temperature and water vapour. Thus, in this idealised case, the prior information was perfect, except for aerosol.

AMTD
6, 9397–9465, 2013

Figure 13 presents histograms for the differences between the retrieved X_{CO_2} and X_{CH_4} and the truth, the latter adjusted for the averaging kernel in the case of CO_2. The rows show results for CO_2, CH_4 and CO, while the columns represent the baseline and descope options. The broader histograms in grey show the scatter before the application of the post-processing filter (PPF), whose specification is provided in Table 5. The narrower histograms in colour show the scatter after the PPF.

The bias (b) and standard deviation (s) of the filtered histograms, indicated on the plots, are comfortably within the tolerances set for the baseline mission, 0.7 % for X_{CO_2}, 1 % for X_{CH_4} and 10 % for X_{CO}. For all three trace gases, the baseline performance clearly is superior. Nevertheless, the threshold mission requirements still can be met with the cheaper descope options.

The importance of the PPF also is clear in Fig. 13. For example, for CO_2 and the baseline configuration of geoCARB, the mean and standard deviation of all soundings rise to −2.4 ppm and 8.9 ppm, well outside the geoCARB specification. As mentioned previously, the PPF is needed principally because the representations of cloud and aerosol within the forward model are incompatible with reality, and therefore the model either cannot fit the spectra or does so by assigning improbable values to other physical variables.

5.3 Experiment 2 – geoCARB retrievals with perfect meteorology and imperfect trace gas priors

In the second experiment, the prior profiles assigned to CO_2, CH_4 and CO differ from the truth, but the prior meteorology is still locked to the truth. For CO_2, the prior profile is the same as that used by O'Dell et al. (2012) in their study for GOSAT. For CH_4 and CO the prior profiles are fixed across the globe, and the retrieval algorithm adjusts only a scaling factor for each gas when attempting to match models to observations. Because the vertical distribution of CO, and to a lesser extent that of CH_4, can vary strongly depending upon local sources, it is to be expected that using a single prior will add to both the bias and the scatter of the retrieved mixing ratios relative to the truth.

AMTD
6, 9397–9465, 2013

The effect will be larger the more the averaging kernel deviates from a being constant with height.

The prior profiles for CH_4 and CO, shown as heavy black lines in Fig. 14, are from the MOZART chemical transport model, and are meant to describe "transport" scenarios. For comparison, the fine coloured lines in Fig. 14 are the profiles of CH_4 and CO encountered along one of the orbits used in the simulations. Clearly the prior for CO is not a good choice, because it has a peak in the upper troposphere whereas the true profiles peak near the surface, probably indicating surface sources of CO. Thus, retrievals with this fixed prior should represent a near worst case scenario.

The upper row of Fig. 15 compares the prior values of X_{CO_2}, X_{CH_4} and X_{CO} with their true values, and therefore indicates the spread within the ensemble of scenes generated along the orbits of Fig. 5. For CO_2 and CH_4 the priors are quite tight, perhaps too tight, while for CO the prior deviates significantly from the truth. Generally the prior values of CO are too low, so we anticipate that the retrieved X_{CO} also will be low.

The middle row of Fig. 15 shows the errors in the column amounts retrieved with the approximate prior profiles. The results are for the baseline configuration of geoCARB, and the meteorology coincides with the truth; the bottom row (experiment 3 below) has approximate meteorology in addition to approximate prior profiles. Despite the larger scatter than in experiment 1, the mission targets are still met comfortably for CO_2 and CH_4, and marginally for CO. In practice, ancillary data would be used to provide better priors.

5.4 Experiment 3 – geoCARB retrievals with imperfect meteorology and imperfect trace gas priors

The assumption of perfect meteorology was relaxed in the third experiment. The prior for the surface pressure was obtained by adding to the true surface pressure a random offset drawn from a gaussian distribution with mean zero and standard deviation 2 hPa. Similarly, the prior temperature profile was generated by adding to the true profile a random offset, constant with height, drawn from a gaussian distribution with mean zero and

AMTD
6, 9397–9465, 2013

standard deviation 2 K. The prior distribution for the water vapour profile remained at the truth. For each of the variables (surface pressure, temperature and water vapour), the initial guess in the retrieval algorithm was identical to the prior.

The impact of imperfect knowledge of the meteorology is shown in the lower row of Fig. 15 for the baseline configuration of geoCARB. Significantly, the biases and standard deviations of the error distributions for all three gases are almost identical to those in experiment 2, which was conducted with perfect meteorology. It is fair to conclude that realistic uncertainties in the meteorology are not a serious source of error.

5.5 Power plant emissions

The field of regard of geoCARB at longitude 110° E includes many large power plants, as indicated in Fig. 16, where the magenta and green points respectively denote plants with annual emissions in the range 5–15 Mt CO_2 yr^{-1} and greater than 15 Mt CO_2 yr^{-1}. According to the Carbon Monitoring for Action (CARMA) data base (CARMA, 2012), power plants with emission rate greater than 5 Mt CO_2 yr^{-1} comprise approximately 60 % of the emission budget for the box between 60° E and 160° E longitude and 45° S and 65° N latitude, roughly corresponding to the field of regard of geoCARB. The shading in Fig. 16 indicates the growth of the geoCARB pixel area with distance from the sub-satellite point, where the area is 12.25 km^2. The majority of the large plants fall within the region where the pixel area is less than a factor of two larger than the sub-satellite pixel (linear dimension no more than $\sqrt{2}$ larger).

Bovensmann et al. (2010b) demonstrated that instantaneous CO_2 emissions from power plants could be estimated with good accuracy using spectra from CarbonSat, especially when the wind speed is low. CarbonSat has a push-broom scanner with a 500 km swath, and therefore can image an extensive area around a power plant on each overpass. Because the plume of CO_2 from a power plant should stand out against the background, the strength of the emissions may be estimated even in the presence of consistent biases in the retrieved X_{CO_2}. Observations from GEO offer an additional

AMTD
6, 9397–9465, 2013

advantage, because the region around a power plant can be scanned multiple times in quick succession, thereby improving the statistics of the observation. For example, geoCARB has the ability to acquire up to ten snap-shots per hour in a dedicated target mode. Alternatively, the snap-shots could be spread over a longer period if the emissions may be assumed to be steady, but this also requires that the meteorology can be modelled well.

In this section we present two results for geoCARB. The first is an analytical estimate of the number of images required to achieve a nominated accuracy for plant emissions. Its value is that it sets a benchmark that avoids most of the specific instrument details. The second involves retrievals of plant emission rates from simulated geoCARB spectra, and illustrates the advantage of fine temporal sampling with subsequent averaging of multiple snap-shots.

5.5.1 An analytical estimate

In this subsection we estimate the number of observations of a gaussian plume required to achieve a specified accuracy for the rate of emission of CO_2 from a power plant, given as input that individual measurements of X_{CO_2} are subject to random error. Both the plume and the emission rate of the power plant are assumed to be constant in time.

Assume that the enhancement $\Delta(x,y)$ of the column of CO_2 at point (x,y) caused by the plume is described by a stationary gaussian plume,

$$\Delta(x,y) = \frac{q}{u}\frac{1}{\sqrt{2\pi}s(x)}\exp\left[-\frac{y^2}{2s(x)^2}\right], \quad (5)$$

where q is the emission rate, assumed constant in time, u is the wind speed along the x-axis, also assumed constant in time, and $s(x)$ describes how the plume spreads in

AMTD
6, 9397–9465, 2013

the cross-wind direction. The X_{CO_2} field observed by geoCARB will be

$$P(x,y) = \int L(x - x_0, y - y_0)\Delta(x_0, y_0)\,\mathrm{d}x_0\,\mathrm{d}y_0, \tag{6}$$

where $L(x,y)$ is point spread function for geoCARB.

Further assume that the error associated with each measurement, denoted ε, is normally distributed with mean zero, variance σ_ε^2 and probability density

$$p(\varepsilon) = \frac{1}{\sqrt{2\pi}\sigma_\varepsilon} \exp\left[-\frac{\varepsilon^2}{2\sigma_\varepsilon^2}\right]. \tag{7}$$

Assume that the distribution is independent of position within the domain containing the power plant. The measured X_{CO_2} then will be

$$W(x,y) = P(x,y) + \varepsilon. \tag{8}$$

If errors in the meteorology and the distribution of the plume are either negligible or ignored, then the ratio q/u can be estimated by minimizing the cost function

$$J(q/u, B) = \sum_k \left[W(x_k, y_k) - (q/u)S(x_k, y_k) - B\right]^2, \tag{9}$$

where B denotes the background level of X_{CO_2}, k indexes the pixels within the domain surrounding the power plant, and

$$S(x,y) = \int \frac{L(x - x_0, y - y_0)}{\sqrt{2\pi}s(x_0)} \exp\left[-\frac{y_0^2}{2s(x_0)^2}\right] \mathrm{d}x_0\,\mathrm{d}y_0. \tag{10}$$

Because ϵ is an independent random variable, uncorrelated from pixel to pixel, we can estimate the error in q, obtaining

$$\sigma_q = \frac{u\sigma_\varepsilon}{\sqrt{M(\langle S(x_k,y_k)^2\rangle - \langle S(x_k,y_k)\rangle^2)}}, \tag{11}$$

AMTD
6, 9397–9465, 2013

where M is the number of pixels in the domain and the angle brackets denote mean values.

If all observations of the power plant are statistically independent, we can estimate the number N of images that must be collected to reduce the error in q to any specified level. For example, if the required error in the emission rate is $1\,\mathrm{Mt\,CO_2\,yr^{-1}}$, then the number of samples required is

$$N = \frac{(u\sigma_\varepsilon)^2}{M(\langle S(x_k,y_k)^2\rangle - \langle S(x_k,y_k)\rangle^2)}. \quad (12)$$

This simple formula shows that the required number of measurements increases quadratically with the error of a single X_{CO_2} measurement, thus placing a difficult constraint on missions using sun-synchronous satellites, since such missions provide only limited observations of the same real estate. In contrast a geostationary orbit enables multiple observations (certainly several times per day), and therefore may tolerate higher error in each X_{CO_2} measurement. Continuing the example for geoCARB observation geometry with wind from the west at $5\,\mathrm{m\,s^{-1}}$ and X_{CO_2} error σ_ε at 3 ppm[4], the number of images required to achieve an accuracy of $1\,\mathrm{Mt\,CO_2\,yr^{-1}}$ is as shown in Fig. 17, expressed as a function of the latitude or longitude difference $\Delta\theta$ from the sub-satellite point. The limiting value is 42 at the SSP. This number should be compared with potential 1095 observations per year (three times a day) planned for the geoCARB mission. With targeted sampling, the number of observations could be much higher. The marked difference between the curves for looking east-west vs. north-south arises because the wind direction happens to be from the west. As the footprint increases in size with distance from the SSP, the corresponding smearing along the wind direction does less harm than smearing across the wind direction. In general with an arbitrary wind

[4] An error of 3 ppm is slightly higher than the mission target for geoCARB, which at 0.7 % and the current volume mixing ratio of 395 ppm translates to 2.8 ppm. The error of GOSAT estimates of X_{CO_2} is presently better than 3 ppm.

AMTD
6, 9397–9465, 2013

direction, the number of snap-shots required will lie between the two curves shown in Fig. 17.

5.5.2 Estimating power plant emissions

Simulations were performed for a gaussian plume as described by Eq. (5). Following Bovensmann et al. (2010b), we assumed that the spread in the cross-wind direction $s(x)$ may be parameterised in the form

$$s(x) = a[(x + x_0)/L]^b,$$

with the parameter values

$$a = 0.104\,\text{km}, \quad L = 1\,\text{km}, \quad b = 0.894 \quad \text{and} \quad x_0 = 0.1\,\text{km}.$$

For the initial tests, the emission rate was assumed to be $q = 13\,\text{Mt}\,\text{CO}_2\,\text{yr}^{-1}$, and the wind was assumed to be light with speed $u = 1\,\text{m}\,\text{s}^{-1}$ blowing from the west[5].

Radiance spectra were simulated at the top of the atmosphere in all bands of the baseline configuration of geoCARB. Two scenarios were considered. In the first, the aerosol background was assumed to be uniform with optical thickness 0.25 at the blue end of the O_2 A-band. The aerosol was a mixture of water cloud and smoggy aerosol. The underlying surface albedo in each of the bands was assumed to be spatially uniform over the target area, with respective values of approximately 0.21, 0.30, 0.22 and 0.21 at the band centres. In the second scenario, the power plant was assumed

[5]In practice the wind will be flukey at such low speeds, and its direction and the geometry of the plume will be hard to predict, For example, Karion et al. (2013) found that low, variable, and sometimes recirculating winds in the 0.5–1.5 $\text{m}\,\text{s}^{-1}$ range made an analysis of the mass balance for CH_4 emissions almost impossible. The value of the present study with low wind speed is simply that the enhancements of X_{CO_2} are larger and the importance of averaging is more easily seen. Cases with higher wind speed will be considered later.

AMTD
6, 9397–9465, 2013

to inject aerosol into the column, the amount being proportional to the CO_2 enhancement. Where the X_{CO_2} enhancement was largest, the aerosol optical depth was increased by 0.15 above the background. The first scenario is appropriate for a modern coal-fired power plant with efficient scrubbers on the stack, while the second is more representative of older, more polluting plants.

The upper and lower panels in the left-hand column of Fig. 18 show the retrieved enhancement of X_{CO_2} above the background caused by the power plant and the difference between the retrieved and true enhancements. The results are for the first scenario, representing a clean power plant, and are based upon analysis of a single snap-shot by geoCARB. The retrieved plume is clearly visible against the background, and the emission rate estimated from the snap-shot is very close to the truth (Table 7).

The panels in the middle and right-hand columns of Fig. 18 are similar, except that the emission estimates from respectively three and ten snap-shots have been averaged. With increased averaging, the random errors partially cancel, the plume is more clearly defined against the background, and the emission estimates are close to the truth (Table 7). This is true despite the fact that the retrieved X_{CO_2} is biased low by approximately 0.5 ppm for all snap-shots.

The second scenario, representing a power plant whose plume contains aerosol, is more complex. Figure 19 is qualitatively similar to Fig. 18 for the clean power plant, but, as the right-hand columns of Table 7 show, the estimates of the emission strength are consistently low by approximately 14 %. The magnitude of the bias presumably depends upon the type and amount of aerosol emitted by the power plant, but more research is needed to quantify this effect.

Lastly, Fig. 20 shows the retrieved plumes after averaging ten snap-shots for wind speeds of $5\,m\,s^{-1}$ and $10\,m\,s^{-1}$, all for the scenario of a clean power plant with no aerosol emissions. The corresponding estimates for the emission strength are displayed in Table 7. Thus, even for higher wind speeds, when the the CO_2 enhancement is smaller, the plume is visible against the background in the average of several

AMTD
6, 9397–9465, 2013

snap-shots. Furthermore, the estimate for the rate of emission remains accurate in the average.

For every pixel in the simulations, the total optical thickness of aerosol varied between 0.25 and 0.40, which would exceed the threshold for aerosol optical thickness defined earlier for the post-processing filter. Therefore, no PPF was applied for this power plant study.

In practice cloud often will obscure some of the pixels in the snap-shots, so it might be argued that the results in Fig. 18 are too optimistic. In order to investigate the effect of cloud, we generated a random mask that excluded a prescribed fraction of pixels from each snap-shot, and then estimated the emission rate of the plant with the remaining unmasked pixels. We repeated the exercise for 1001 random realisations of the mask, and constructed a histogram of the error in the estimated emission rate.

The results are presented in Fig. 21 for cloud fractions of 10, 50, 80, 90 and 95 %. In all cases, the mean value of the error is close to zero, while the standard deviation grows steadily with the cloud fraction. Even for the case with 95 % of the pixels obscured, the standard deviation is only 1.19 $Mt\,CO_2\,yr^{-1}$, or approximately 9 % of the true emission rate of 13 $Mt\,CO_2\,yr^{-1}$. The important message from this calculation is that geoCARB, with its rapid and contiguous sampling, will provide so many samples that the loss of a large fraction can be tolerated without significantly degrading the accuracy of emission estimates.

5.6 A case study – Karimnagar, India

In a first attempt to move beyond idealised studies to a difficult but realistic scenario, we selected a large power station in India at Karimnagar and simulated spectra at the top of the atmosphere for the baseline configuration of geoCARB on the winter solstice for local times of 08:00, 12:00 and 16:00 h. The scanning pattern and footprints of geoCARB were modelled carefully, so the correct sun and satellite geometry was used. The surface properties were derived from MODIS and POLDER, as described earlier, at 1 km spatial resolution throughout the target region of 51 × 51 geoCARB pixels. The

AMTD
6, 9397–9465, 2013

optical properties and vertical distributions of cloud and aerosol were extracted randomly for each pixel from the CALIPSO collection of profiles for the $2^\circ \times 2^\circ$ box containing Karimnagar for the month of December. No attempt was made to correlate either clouds or aerosols spatially; each pixel was an independent sample. The meteorology was interpolated in time and space from three-hourly ECMWF forecasts to each pixel within the target area, but no adjustment was made for topography. Profiles of CO_2, CH_4 and CO were extracted for Karimnagar from the PCTM, TM4 and MOPITT data bases. As the spatial resolutions of the models were too coarse to provide structure within the 51×51 target region, the values of X_{CO_2}, X_{CH_4} and X_{CO} for each pixel were incremented by random numbers drawn from uniform distributions with standard deviations of 3 ppm, 100 ppb and 10 ppb respectively. The reference profiles then were scaled to have the simulated column amounts. In the retrievals all pixels used the average of the true profiles over the target region as the prior estimates. Because the simulations used 92 levels of the ECMWF forecasts, while the retrievals required that the prior profile be specified on only 20 levels, additional small differences between the prior profiles and the truth were introduced by the interpolation from 92 to 20 levels.

This target is challenging.

Firstly, the aerosol loading is high, as shown (for local time 12:00) in the left-hand panel of the upper row of Fig. 22. The histograms show the total AOD at the blue end of the O_2 A-band both before and after the PPF. The throughput of the PPF is only 8.1 %, and, importantly, includes a significant fraction of cases where the true (as distinct from the retrieved) AOD exceeds the threshold of 0.1 set in the PPF. Eliminating such cases with a better screen for cloud, such as the pre-filter used for GOSAT, would improve the accuracy of the retrieved gas amounts. The middle and right-hand panels of the upper row of Fig. 22 respectively show the spatial distribution of AOD for retrievals that converged and those that passed the PPF. The thinning seen in the latter is likely to be typical of the world seen by geoCARB. However, as argued above in Fig. 21 where pixels were discarded randomly to imitate the effect of cloud, reliable estimation

AMTD
6, 9397–9465, 2013

of emission strengths remains feasible, because the initial density of observations is so high.

Secondly, the airmass is high, with mean values over the target area of 4.92, 2.80 and 4.26 at 08:00, 12:00 and 16:00 h. For reference it should be noted that the retrieval algorithm for GOSAT rejects soundings with airmass greater than 2.7, so all of the soundings over Karimnagar would be rejected.

The lower row of Fig. 22 presents histograms of the errors for the retrieved X_{CO_2}, X_{CH_4} and X_{CO}. The PPF screens all but 8.1 % of the pixels in the target area, but those that pass the filter meet the mission targets. In practice priors further from the truth for the trace gas profiles and the meteorology are likely to increase the errors, but experiments 2 and 3 described earlier suggest that these errors will not compromise the mission.

The simulations at 08:00 and 16:00 (not plotted) return biases for X_{CO_2} of 1.1 ppm and 1.3 ppm, considerably higher than the almost unbiased estimate at noon. Nevertheless, these values, obtained with air mass factors of 4.92 and 4.26, still fall within the acceptable range for geoCARB. Furthermore, the PPF passed 17 % and 20 % of the soundings at 08:00 and 16:00, despite the adverse geometry at the time of the winter solstice.

6 Conclusions

The accuracy of X_{CO_2}, X_{CH_4} and X_{CO} estimated from geoCARB spectra was tested using end-to-end simulations and retrievals with realistic meteorology, aerosol, cloud and surface properties. The respective target accuracies of 0.7, 1 and 10 % were met for the baseline configuration of geoCARB when a generic post-processing filter was applied to eliminate soundings where the differences between the fitted and simulated spectra consistently exceeded the noise. This result is robust. It holds even when the prior profiles for the trace gases differ from the true profiles in ways that are likely to occur in practice. Similarly, plausible uncertainties in the meteorology used in the

AMTD
6, 9397–9465, 2013

retrieval algorithm introduce only small (and acceptable) errors in the retrieved trace gas concentrations.

Two descope options were considered. Both sacrifice the LW spectrometer bands at 2.065 µm and 2.323 µm. The impact of losing the strong CO_2 band at 2.065 µm was examined in the context of GOSAT using both simulated and real data. By increasing the noise assigned to the strong CO_2 channels, its impact on retrievals was reduced to essentially nil. With decreasing significance of the strong CO_2 band, the bias in retrieved X_{CO_2} became increasingly negative, and the correlation between errors in X_{CO_2} and errors in surface pressure weakened. The results for GOSAT used an older version of the retrieval code, and appear more pessimistic than end-to-end tests for the descope options of geoCARB. Overall, descoping the strong CO_2 band provides an acceptable level of performance for X_{CO_2} and X_{CH_4} at a significantly reduced cost. However, the ability to classify sources of CO_2 is impaired by the loss of the CO channel at 2.323 µm.

The contiguous sampling and fine temporal resolution possible with geoCARB enable rates of emission from power plants to be estimated. For plants with particulate filters on their stacks to reduce (or eliminate) aerosol emissions, the accuracy is approximately 3 % when the plume of the power plant is observed against a uniform background. To achieve this level of accuracy, ten snap-shots of the power plant were averaged. In practice, ten images could be acquired within an hour if geoCARB is operated in a dedicated target mode. The error increases with the wind speed, but does not exceed 3 % for wind speeds up to 10 $m\,s^{-1}$.

For dirty power plants that emit aerosol in the plume, adding a maximum of 0.15 to the optical thickness in proportion to the CO_2 enhancement, the estimates from successive snap-shots were biased low by approximately 14 %, although the scatter between the estimates remained less than 2.5 %.

The power plant results are robust. They continue to hold in the presence of high proportions of cloud; with 95 % of the pixels masked by cloud, the standard deviation of emission rate estimates rose only to 9 %, while the mean remained accurate. Thus,

AMTD
6, 9397–9465, 2013

with the large number of observations possible from GEO, estimating current emission rates accurately should be possible.

Simulations for the region surrounding a real power plant (Karimnagar in India) highlighted the importance of the robustness to cloud and aerosol. The simulations were for the winter solstice when the aimass is high. The fraction of pixels passing the post-processing filter was low (only 8.1 % at noon), but the bias and scatter of pixels that pass the PPF remain low. This result again emphasises that repeated sampling in rapid succession will allow the error in the average to be brought within the mission requirements, even for adverse conditions with high air mass.

Acknowledgements. Polonsky and Kumer were funded for this work by the Lockheed-Martin corporation. The authors gratefully acknowledge that many aspects of this work are the outcome of close collaboration with the geoCARB team, who provided many valuable insights.

References

Baum, B. A., Heymsfield, A. J., Yang, P., and Bedka, S. T.: Bulk scattering properties for the remote sensing of ice clouds, Part 1: Microphysical data and models, J. Appl. Meteorol., 44, 1885–1895, doi:10.1175/JAM2308.1, 2005a. 9406

Baum, B. A., Yang, P., Heymsfield, A. J., Platnick, S., King, M. D., Hu, Y.-X., and Bedka, S. T.: Bulk scattering properties for the remote sensing of ice clouds, Part 2: Narrowband models, J. Appl. Meteorol., 44, 1896–1911, doi:10.1175/JAM2309.1, 2005b. 9406

Bovensmann, H., Buchwitz, M., and Burrows, J. P.: Carbon monitoring satellite (CarbonSat) as an Earth Explorer Opportunity Mission: mission overview, available at: http://www.iup.uni-bremen.de/carbonsat (last access: 29 October 2013), 2010a. 9399

Bovensmann, H., Buchwitz, M., Burrows, J. P., Reuter, M., Krings, T., Gerilowski, K., Schneising, O., Heymann, J., Tretner, A., and Erzinger, J.: A remote sensing technique for global monitoring of power plant CO_2 emissions from space and related applications, Atmos. Meas. Tech., 3, 781–811, doi:10.5194/amt-3-781-2010, 2010b. 9399, 9402, 9421, 9425

CARMA: Carbon Monitoring for Action, available at: http://carma.org (last access: 29 October 2013), 2012. 9421

AMTD
6, 9397–9465, 2013

Connor, B. J., Boesch, H., Toon, G., Sen, B., Miller, C., and Crisp, D.: The Orbiting Carbon Observatory (OCO): inverse method and prospective error analysis, J. Geophys. Res., 113, D05305, doi:10.1029/2006JD008336, 2008. 9410

Crisp, D., Atlas, R., Breon, F.-M., Brown, L. R., Burrows, J., Ciais, P., Connor, B. J., Doney, S. C., Fung, I. Y., Jacob, D. J., Miller, C. E., O'Brien, D., Pawson, S., Randerson, J. T., Rayner, P., Salawitch, R. J., Sander, S. P., Sen, B., Stephens, G. L., Tans, P. P., Toon, G. C., Wennberg, P. O., Wofsy, S. C., Yung, Y. L., Kuang, Z., Chudasama, B., Sprague, G., Weiss, B., Pollock, R., Kenyon, D., and Schroll, S.: The Orbiting Carbon Observatory (OCO) mission, Adv. Space Res., 34, 700–709, doi:10.1016/j.asr.2003.08.062, 2004. 9401

Crisp, D., Fisher, B. M., O'Dell, C., Frankenberg, C., Basilio, R., Bösch, H., Brown, L. R., Castano, R., Connor, B., Deutscher, N. M., Eldering, A., Griffith, D., Gunson, M., Kuze, A., Mandrake, L., McDuffie, J., Messerschmidt, J., Miller, C. E., Morino, I., Natraj, V., Notholt, J., O'Brien, D. M., Oyafuso, F., Polonsky, I., Robinson, J., Salawitch, R., Sherlock, V., Smyth, M., Suto, H., Taylor, T. E., Thompson, D. R., Wennberg, P. O., Wunch, D., and Yung, Y. L.: The ACOS CO_2 retrieval algorithm – Part II: Global X_{CO_2} data characterization, Atmos. Meas. Tech., 5, 687–707, doi:10.5194/amt-5-687-2012, 2012. 9400, 9416

Deeter, M. N., Emmons, L. K., Francis, G. L., Edwards, D. P., Gille, J. C., Warner, J. X., Khattatov, B., Ziskin, D., Lamarque, J.-F., Ho, S.-P., Yudin, V., Attié, J.-L., Packman, D., Chen, J., Mao, D., and Drummond, J. R.: Operational carbon monoxide retrieval algorithm and selected results for the MOPITT instrument, J. Geophys. Res., 108, 4399, doi:10.1029/2002JD003186, 2003. 9407, 9449

Deeter, M. N., Edwards, D. P., and Gille, J. C.: Retrievals of carbon monoxide profiles from MOPITT observations using lognormal a priori statistics, J. Geophys. Res., 112, 11311, doi:10.1029/2006JD007999, 2007a. 9407, 9449

Deeter, M. N., Edwards, D. P., Gille, J. C., and Drummond, J. R.: Sensitivity of MOPITT observations to carbon monoxide in the lower troposphere, J. Geophys. Res., 112, 24306, doi:10.1029/2007JD008929, 2007b. 9407, 9449

Dubovik, O., Holben, B., Eck, T. F., Smirnov, A., Kaufman, Y. J., King, M. D., Tanré, D., and Slutsker, I.: Variability of absorption and optical properties of key aerosol types observed in worldwide locations, J. Atmos. Sci., 59, 590–608, 2002. 9406

EDGAR: Emissions Database for Global Atmospheric Research, available at: http://edgar.jrc.ec.europa.eu/index.php (last access: 29 October 2013), 2011. 9401

AMTD
6, 9397–9465, 2013

Frankenberg, C., Platt, U., and Wagner, T.: Iterative maximum a posteriori (IMAP)-DOAS for retrieval of strongly absorbing trace gases: Model studies for CH_4 and CO_2 retrieval from near infrared spectra of SCIAMACHY onboard ENVISAT, Atmos. Chem. Phys., 5, 9–22, doi:10.5194/acp-5-9-2005, 2005. 9411

Gerilowski, K., Tretner, A., Krings, T., Buchwitz, M., Bertagnolio, P. P., Belemezov, F., Erzinger, J., Burrows, J. P., and Bovensmann, H.: MAMAP – a new spectrometer system for column-averaged methane and carbon dioxide observations from aircraft: instrument description and performance analysis, Atmos. Meas. Tech., 4, 215–243, doi:10.5194/amt-4-215-2011, 2011. 9399

Heidinger, A. K., O'Dell, C., Bennartz, R., and Greenwald, T.: The successive-order-of-interaction radiative transfer model: Part 1: Model development, J. Appl. Meteorol. Clim., 45, 1388–1402, doi:10.1175/JAM2387.1, 2006. 9408

Ivanova, D., Mitchell, D. L., Arnott, W. P., and Poellot, M.: A GCM parameterization for bimodal size spectra and ice mass removal rates in mid-latitude cirrus clouds, Atmos. Res., 59–60, 89–113, doi:10.1016/S0169-8095(01)00111-9, 2001. 9406

Kahn, R., Banerjee, P., and McDonald, D.: Sensitivity of multiangle imaging to natural mixtures of aerosols over ocean, J. Geophys. Res., 106, 18219–18238, 2001. 9410

Karion, A., Sweeney, C., Pétron, G., Frost, G., Hardesty, R. M., Kofler, J., Miller, B. R., Newberger, T., Wolter, S., Banta, R., Brewer, A., Dlugokencky, E., Lang, P., Montzka, S. A., Schnell, R., Tans, P., Trainer, M., Zamora, R., and Conley, S.: Methane emissions estimate from airborne measurements over a western United States natural gas field, Geophys. Res. Lett., 40, 4393–4397, doi:10.1002/grl.50811, 2013. 9425

Kawa, S. R., Erickson, D. J., Pawson, S., and Zhu, Z.: Global CO_2 transport simulations using meteorological data from the NASA data assimilation system, J. Geophys. Res., 109, 18312, doi:10.1029/2004JD004554, 2004. 9407

Krings, T., Gerilowski, K., Buchwitz, M., Reuter, M., Tretner, A., Erzinger, J., Heinze, D., Pflüger, U., Burrows, J. P., and Bovensmann, H.: MAMAP – a new spectrometer system for column-averaged methane and carbon dioxide observations from aircraft: retrieval algorithm and first inversions for point source emission rates, Atmos. Meas. Tech., 4, 1735–1758, doi:10.5194/amt-4-1735-2011, 2011. 9399

Krol, M., Houweling, S., Bregman, B., van den Broek, M., Segers, A., van Velthoven, P., Peters, W., Dentener, F., and Bergamaschi, P.: The two-way nested global chemistry-

AMTD
6, 9397–9465, 2013

transport zoom model TM5: algorithm and applications, Atmos. Chem. Phys., 5, 417–432, doi:10.5194/acp-5-417-2005, 2005. 9407

Kumer, J. B., Roche, A. E., Rairden, R. L., Desouza-Machado, S., Blatherwick, R., Hawat, T., and Chatfield, R.: NASA ESTO Instrument Incubator Program (IIP) Tropospheric Infrared Mapping Spectrometers (TIMS): demonstration of multi-layer CO retrieval from atmospheric data acquired simultaneously in the solar reflective region near 2330 nm and the thermal emissive region near 4680 nm, in: Hyperspectral Imaging and Sensing of the Environment, OSA Technical Digest, p. HMC5, Optical Society of America, available at: http://www.opticsinfobase.org/abstract.cfm?URI=HISensE-2009-HMC5 (last access: 29 October 2013), 2009. 9404

Kumer, J. B., Rairden, R. L., Roche, A. E., and Chatfield, R.: NASA ESTO Instrument Incubator Program (IIP) Tropospheric Infrared Mapping Spectrometers (TIMS) demonstration first deployment on an airship: preliminary results, in: Hyperspectral Imaging and Sensing of the Environment, OSA Technical Digest, p. HTuD2, Optical Society of America, available at: http://www.opticsinfobase.org/abstract.cfm?URI=HISE-2011-HTuD2 (last access: 29 October 2013), 2011. 9404

Kumer, J., Rairden, R., and Roche, A.: Modeling the 2.33 µm TIMS spectrometer radiometric noise: implications for space applications, in: Aerospace Conference, 2013 IEEE, 1–20, 2–9 March 2013, Big Sky, MT, USA, doi:10.1109/AERO.2013.6497369, 2013a. 9404

Kumer, J. B., Rairden, R. L., Roche, A. E., Chevallier, F., Rayner, P. J., and Moore III, B.: Progress in development of Tropospheric Infrared Mapping Spectrometers (TIMS): geoCARB green house gas (GHG) application, Proc. SPIE, 8867, 88670K, doi:10.1117/12.2022668, 2013b. 9400

Li, X. and Strahler, A. H.: Geometric-optical bidirectional reflectance modeling of the discrete-crown vegetation canopy: effect of crown shape and mutual shadowing, IEEE T. Geosci. Remote, 30, 276–292, doi:10.1109/36.134078, 1992. 9407

Mobilia, J., Kumer, J. B., Palmer, A., Sawyer, K., Mao, Y., Katz, N., Mix, J., Nast, T., Clark, C. S., Vanbezooijen, R., Magoncelli, A., Baraze, R. A., and Chenette, D. L.: Determination of technical readiness for an atmospheric carbon imaging spectrometer, Proc. SPIE, 8867, 88670L, doi:10.1117/12.2029634, 2013. 9400

O'Brien, D. M., Polonsky, I., O'Dell, C., and Carheden, A.: Orbiting Carbon Observatory (OCO), algorithm theoretical basis document: The OCO simulator, Technical report ISSN 0737-5352-

AMTD
6, 9397–9465, 2013

85, Cooperative Institute for Research in the Atmosphere, Colorado State University, Fort Collins, Colorado, USA, 2009. 9405, 9406

O'Dell, C., Heidinger, A. K., Greenwald, T., Bauer, P., and Bennartz, R.: The successive-order-of-interaction radiative transfer model: Part 2: Model performance and applications, J. Appl. Meteorol. Clim., 45, 1403–1413, doi:10.1175/JAM2409.1, 2006. 9408

O'Dell, C. W.: Acceleration of multiple-scattering, hyperspectral radiative transfer calculations via low-streams interpolation, J. Geophys. Res., 115, D10206, doi:10.1029/2009JD012803, 2010. 9408

O'Dell, C. W., Connor, B., Bösch, H., O'Brien, D., Frankenberg, C., Castano, R., Christi, M., Eldering, D., Fisher, B., Gunson, M., McDuffie, J., Miller, C. E., Natraj, V., Oyafuso, F., Polonsky, I., Smyth, M., Taylor, T., Toon, G. C., Wennberg, P. O., and Wunch, D.: The ACOS CO_2 retrieval algorithm – Part 1: Description and validation against synthetic observations, Atmos. Meas. Tech., 5, 99–121, doi:10.5194/amt-5-99-2012, 2012. 9400, 9410, 9419

Rodgers, C. D.: Inverse methods for atmospheric sounding, vol. 2 of Atmospheric, Oceanic and Planetary Physics, World Scientific, Singapore, 2000. 9409, 9410

Rothman, L. S., Gordon, I. E., Barbe, A., Benner, D. C., Bernath, P. F., Birk, M., Boudon, V., Brown, L. R., Campargue, A., Champion, J.-P., Chance, K., Coudert, L. H., Dana, V., Devi, V. M., Fally, S., Flaud, J.-M., Gamache, R. R., Goldman, A., Jacquemart, D., Kleiner, I., Lacome, N., Lafferty, W. J., Mandin, J.-Y., Massie, S. T., Mikhailenko, S. N., Miller, C. E., Moazzen-Ahmadi, N., Naumenko, O. V., Nikitin, A. V., Orphal, J., Perevalov, V. I., Perrin, A., Predoi-Cross, A., Rinsland, C. P., Rotger, M., Simeckova, M., Smith, M. A. H., Sung, K., Tashkun, S. A., Tennyson, J., Toth, R. A., Vandaele, A. C., and Auwera, J. V.: The HITRAN 2008 molecular spectroscopic database, J. Quant. Spectrosc. Ra., 110, 533–572, doi:10.1016/j.jqsrt.2009.02.013, 2009. 9408

Sawyer, K., Clark, C., Katz, N., Kumer, J., Nast, T., and Palmer, A.: geoCARB instrument design maturity and geostationary heritage, Proc. SPIE, 8867, 88670M, doi:10.1117/12.2024457, 2013. 9400

Taylor, T. E., O'Dell, C. W., O'Brien, D. M., Kikuchi, N., Yokota, T., Nakajima, T. Y., Ishida, H., Crisp, D., and Nakajima, T.: Comparison of cloud screening methods applied to GOSAT near-infrared spectra, IEEE T. Geosci. Remote, 50, 295–309, doi:10.1109/TGRS.2011.2160270, 2012. 9411

AMTD
6, 9397–9465, 2013

Toth, R. A., Brown, L. T., Miller, C. E., Malathy Devi, V., and Benner, D. C.: Spectroscopic database of CO_2 line parameters: 4300–7000 cm^{-1}, J. Quant. Spectrosc. Ra., 109, 906–921, doi:10.1016/j.jqsrt.2007.12.004, 2008. 9408

Velazco, V. A., Buchwitz, M., Bovensmann, H., Reuter, M., Schneising, O., Heymann, J., Krings, T., Gerilowski, K., and Burrows, J. P.: Towards space based verification of CO_2 emissions from strong localized sources: fossil fuel power plant emissions as seen by a CarbonSat constellation, Atmos. Meas. Tech., 4, 2809–2822, doi:10.5194/amt-4-2809-2011, 2011. 9399

VULCAN: Vulcan and Hestia Projects, available at: http://hestia.project.asu.edu (last access: 29 October 2013), 2011. 9401

Wanner, W., Strahler, A. H., Hu, B., Lewis, P., Muller, J.-P., Li, X., Schaaf, C. L. B., and Barnsley, M. J.: Global retrieval of bidirectional reflectance and albedo over land from EOS MODIS and MISR data: theory and algorithm, J. Geophys. Res., 102, 17143–17161, doi:10.1029/96JD03295, 1997. 9407

AMTD
6, 9397–9465, 2013

Table 1. Spectral ranges and resolutions of the geoCARB bands for the baseline and descope options.

Option	Band (μm)	Wavelength range (nm)		Band centre (nm)	Band width (nm)	Dispersion pixel δ (nm)	Resolution $\Delta\lambda$ (nm)	Resolving power $\lambda/\Delta\lambda$
Baseline	0.763	757.9	768.6	763.2	10.7	0.014	0.052	14 677
	1.611	1600.0	1622.5	1611.3	22.5	0.029	0.110	14 648
	2.065	2045.0	2085.0	2065.0	40.0	0.051	0.192	10 762
	2.323	2300.6	2345.6	2323.1	45.0	0.058	0.216	10 741
Descope 1	0.763	757.9	768.6	763.2	10.7	0.014	0.052	14 677
	1.611	1600.0	1622.5	1611.3	22.5	0.029	0.110	14 648
	1.682	1662.5	1702.5	1682.5	40.0	0.051	0.159	10 582
Descope 2	0.763	757.9	768.6	763.2	10.7	0.014	0.052	14 677
	1.635	1599.5	1670.5	1635.0	71.0	0.091	0.280	5839

AMTD
6, 9397–9465, 2013

Table 2. Noise parameters for the geoCARB bands. The units of N_0 and N_1 are nW $(cm^2\ sr\ cm^{-1})^{-1}$.

Option	Band (μm)	N_0	N_1
Baseline	0.763	0.1819	0.003295
	1.611	0.1172	0.002107
	2.065	0.0814	0.001452
	2.323	0.0811	0.001303
Descope 1	0.763	0.1819	0.003295
	1.611	0.1172	0.002107
	1.682	0.0911	0.001592
Descope 2	0.763	0.1819	0.003295
	1.635	0.2068	0.000807

AMTD
6, 9397–9465, 2013

Table 3. Values of $A\cos\theta_s$ such that $N_0^2 = N_1 I$. The table shows that the shot noise limit is reached for very low levels of illumination.

Option	Band	$A\cos\theta_s$
Baseline	0.763	0.0044
	1.611	0.0032
	2.065	0.0034
	2.323	0.0055
Descope 1	0.763	0.0044
	1.611	0.0032
	1.682	0.0026
Descope 2	0.763	0.0044
	1.635	0.0261

AMTD
6, 9397–9465, 2013

Table 4. Parameters determining the spectral sampling.

Option	Band	ν_1 (cm^{-1})	$\delta\nu$ (cm^{-1})	N_b
Baseline	0.763	13 001.5	0.2308	793
	1.611	6163.3	0.1114	778
	2.065	4796.2	0.1167	804
	2.323	4263.3	0.1039	803
Descope 1	0.763	13 001.5	0.2308	793
	1.611	6163.3	0.1114	778
	1.682	5873.7	0.1696	834
Descope 2	0.763	13 001.5	0.2308	793
	1.635	5986.2	0.2996	888

AMTD
6, 9397–9465, 2013

Table 5. Post-processing filters used in the experiments; $\chi^2(\lambda)$ denotes the residual χ^2 for the band with central wavelength λ, AOD denotes the retrieved aerosol optical depth at the blue end of the O_2 A-band, DOF is the number of degrees of freedom for signal in the retrieved profile of CO_2, and $\sigma_p(X)$ denotes the posterior estimate of the error in X.

Baseline	$\chi^2(0.763) + \chi^2(1.611) + \chi^2(2.065) < 2$ AOD < 0.1 DOF > 1.6
Descope 1	$\chi^2(0.763) + \chi^2(1.611) + \chi^2(1.682) < 2$ AOD < 0.1 $\sigma_p(X_{CO_2}) < 0.8$ ppm
Descope 2	$\chi^2(0.763) + \chi^2(1.635) < 2$ AOD < 0.1 $\sigma_p(X_{CO_2}) < 0.8$ ppm

AMTD
6, 9397–9465, 2013

Table 6. Mean and standard deviation of the error in retrieved surface pressure and X_{CO_2} as functions of the amplification of the noise in the strong CO_2 band.

Strong CO_2 band noise amplification	Surface pressure		X_{CO_2}	
	Mean (hPa)	Std dev (hPa)	Mean (hPa)	Std dev (hPa)
1	1.20	2.40	–	–
2	0.77	2.37	−0.81	0.36
4	0.50	2.39	−1.80	0.59
10	0.35	2.42	−2.71	0.74
100	0.29	2.43	−3.06	0.81

AMTD
6, 9397–9465, 2013

Table 7. Power plant emission rate q (in $\mathrm{Mt\,CO_2\,yr^{-1}}$) estimated from ten snap-shots. The columns labelled X_{CO_2} list the estimates for the background X_{CO_2}, whose true value is 374.93 ppm. The true emission rate is 13.0 $\mathrm{Mt\,CO_2\,yr^{-1}}$.

	Clean plume									Dirty plume		
	Wind speed 1 $\mathrm{m\,s^{-1}}$			Wind speed 5 $\mathrm{m\,s^{-1}}$			Wind speed 10 $\mathrm{m\,s^{-1}}$			Wind speed 1 $\mathrm{m\,s^{-1}}$		
Snap-shot	X_{CO_2} (ppm)	q	Error (%)	X_{CO_2} (ppm)	q	Error (%)	X_{CO_2} (ppm)	q	Error (%)	X_{CO_2} (ppm)	q	Error (%)
0	375.47	12.90	−0.8	375.48	12.28	−5.5	375.49	13.75	−5.7	375.46	11.32	−12.9
1	375.48	12.84	−1.2	375.47	12.54	−3.5	375.48	9.58	−26.3	375.49	10.81	−16.8
2	375.48	12.88	−0.9	375.49	12.78	−1.7	375.46	14.99	−15.3	375.46	11.30	−13.1
3	375.50	12.51	−3.8	375.48	13.43	−3.3	375.50	11.67	−10.2	375.51	10.84	−16.6
4	375.47	12.94	−0.5	375.46	12.64	−2.8	375.48	14.23	−9.4	375.46	11.31	−13.0
5	375.48	12.86	−1.1	375.50	12.43	−4.4	375.49	12.42	−4.4	375.47	11.17	−14.1
6	375.49	12.87	−1.0	375.49	11.97	−7.9	375.46	14.34	−10.3	375.46	11.29	−13.1
7	375.49	12.85	−1.1	375.49	11.90	−8.4	375.49	11.17	−14.1	375.47	11.11	−14.5
8	375.48	13.00	−0.0	375.46	12.98	−0.1	375.45	12.52	−3.7	375.47	11.10	−14.7
9	375.48	12.83	−1.3	375.46	12.85	−1.2	375.45	12.98	−0.2	375.44	11.14	−14.3
Avg	375.48	12.85	−1.2	375.48	12.58	−3.2	375.48	12.77	−1.8	375.47	11.14	−14.3

AMTD
6, 9397–9465, 2013

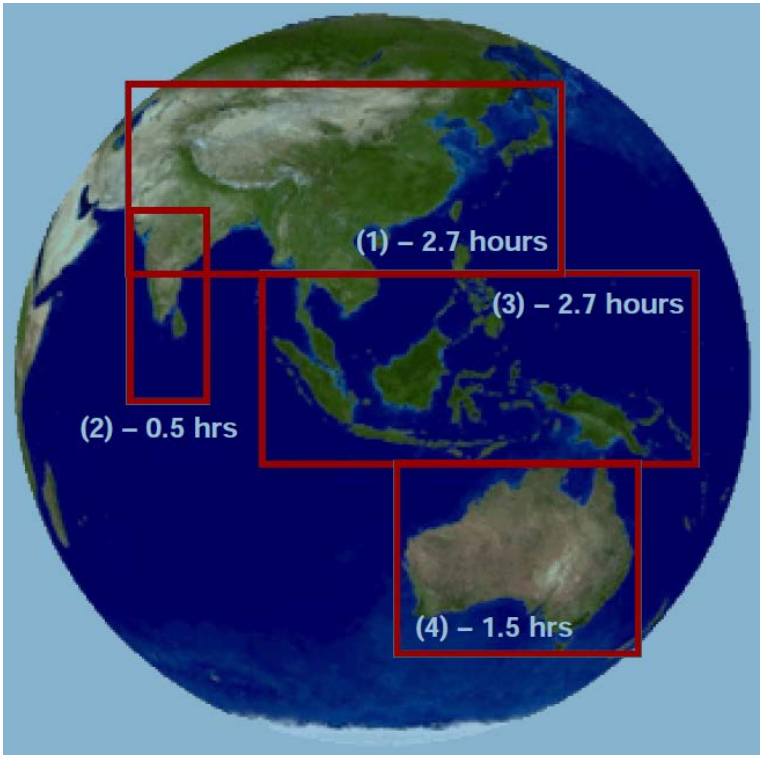

Fig. 1. At 110° E geoCARB scans India, China, Indonesia, Japan and Australia with four scan blocks in less than eight hours.

AMTD
6, 9397–9465, 2013

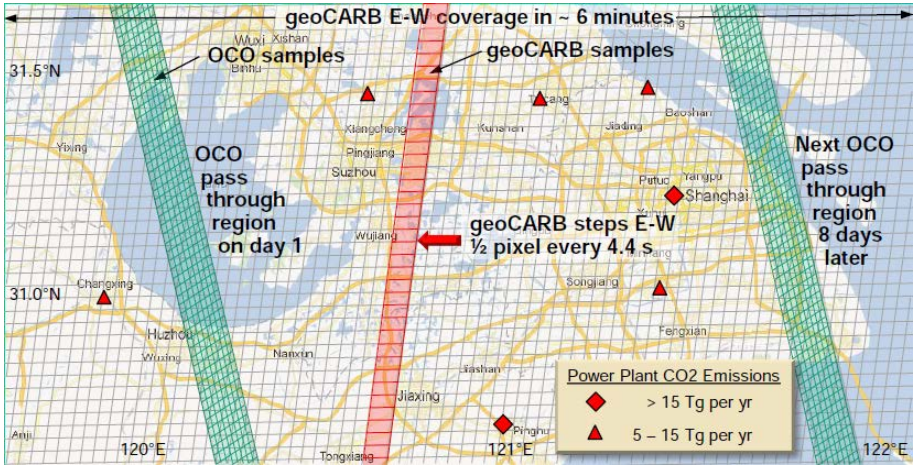

Fig. 2. GeoCARB complements the fine spatial resolution of OCO-2 with contiguous, rapid temporal coverage of any region in the field of regard.

AMTD
6, 9397–9465, 2013

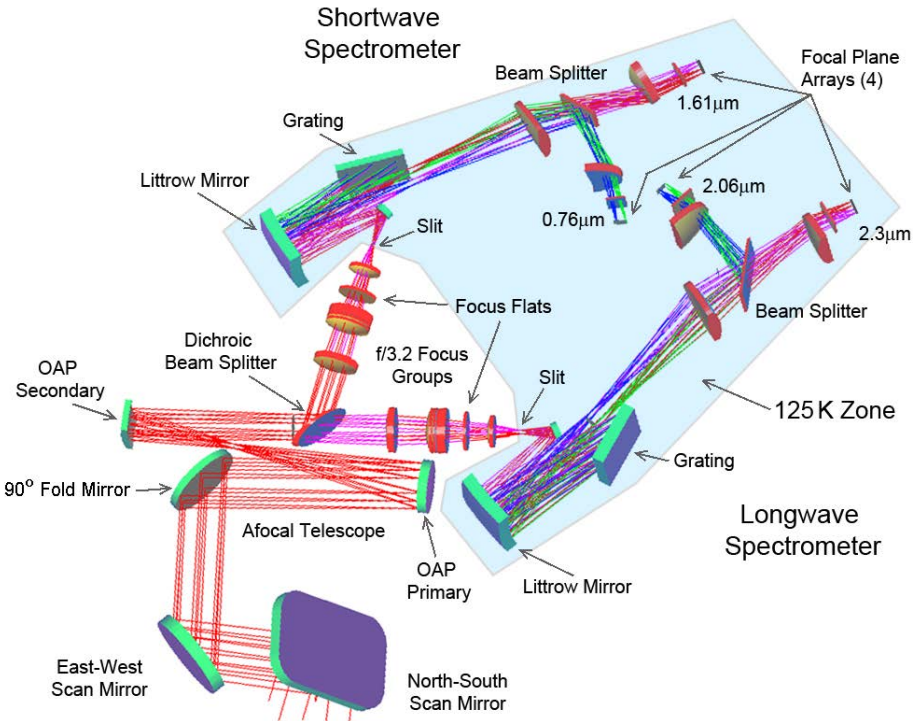

Fig. 3. Optical layout for geoCARB. The primary beam splitter divides the long- and short-wave spectrometer arms. Each Littrow spectrometer feeds two separate focal planes.

AMTD
6, 9397–9465, 2013

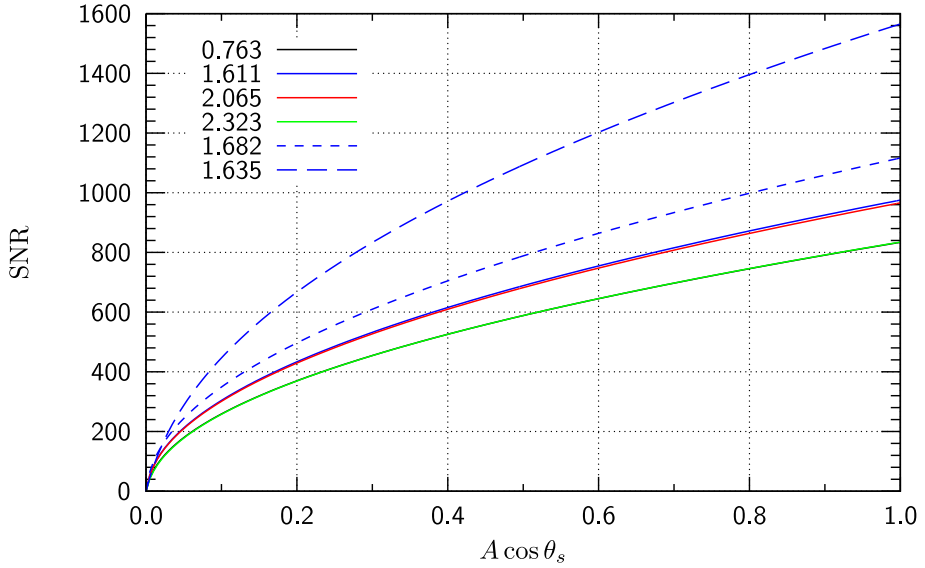

Fig. 4. SNR as a function of $A\cos\theta_s$ for the baseline configuration (solid colours) and for the descope options (dashed). The curves for the bands at 0.763 µm and 2.323 µm by chance are so close as to be indistinguishable.

AMTD
6, 9397–9465, 2013

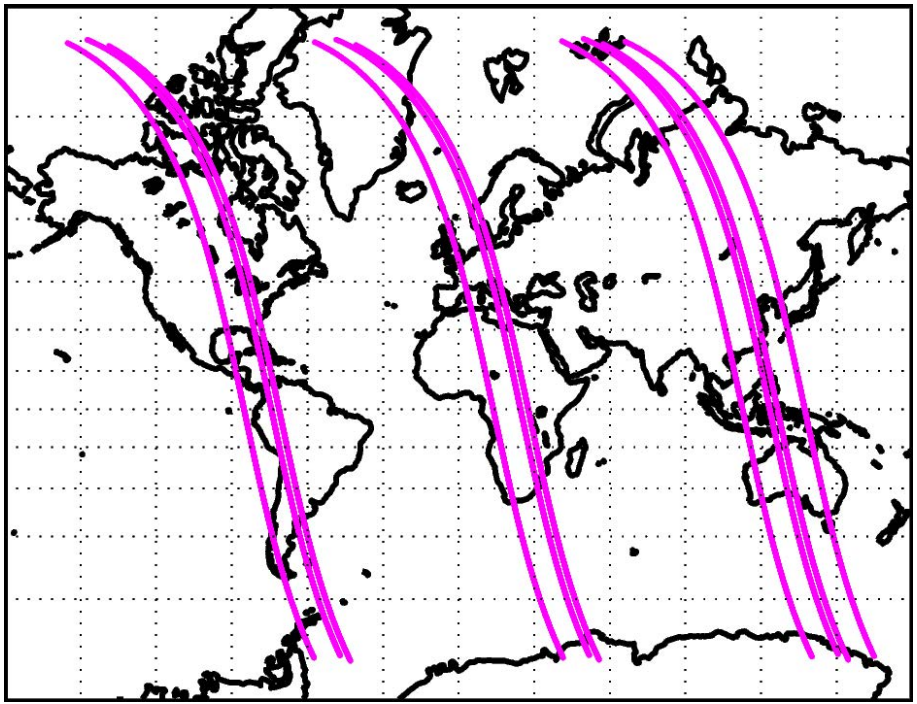

Fig. 5. Polar orbits along which spectra were simulated. Only spectra over land were analysed.

AMTD
6, 9397–9465, 2013

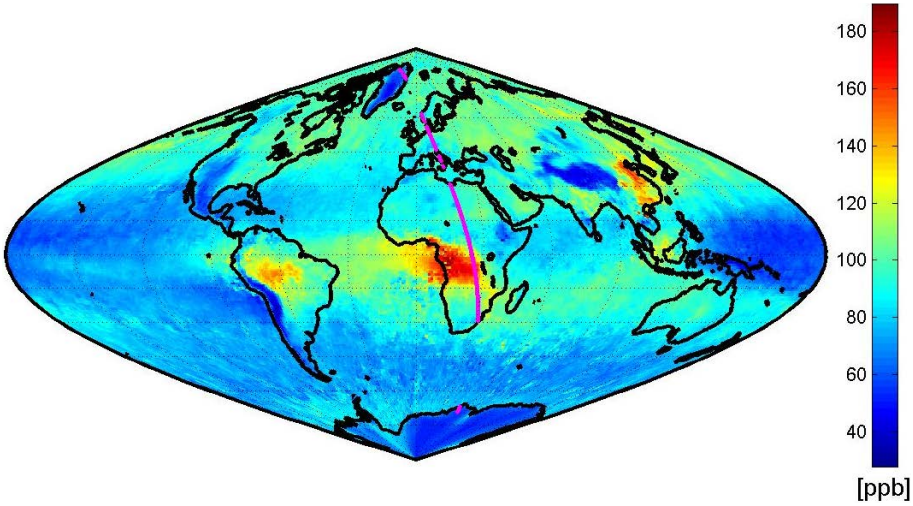

Fig. 6. Global background X_{CO} distribution based on MOPITT data (Deeter et al., 2003, 2007a, b). The magenta line shows the projection of the land portion of just one of the orbits used in the simulation.

AMTD
6, 9397–9465, 2013

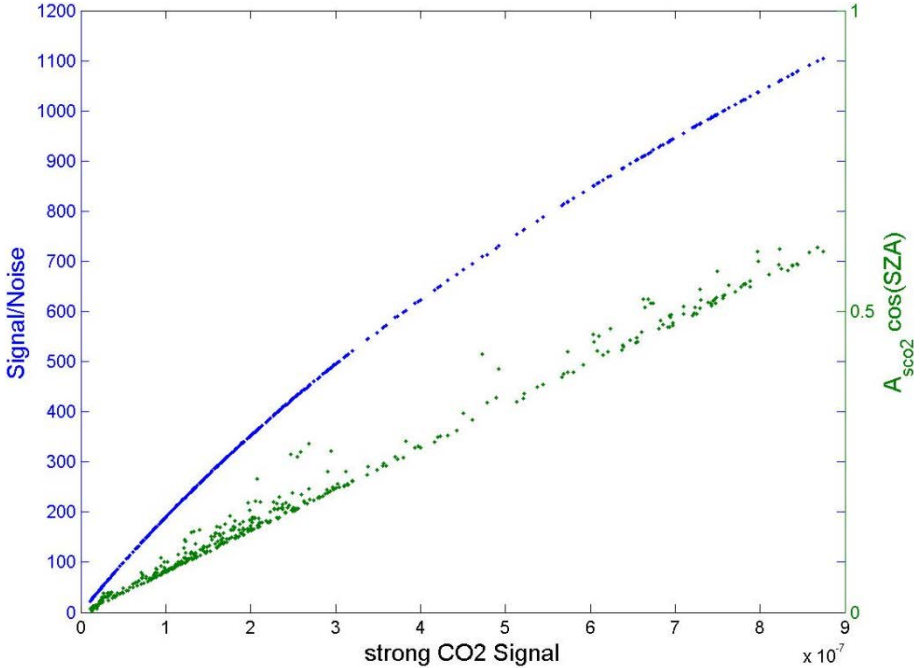

Fig. 7. Signal-to-noise model for GOSAT in the strong CO_2 band. The points correspond to samples along one of the orbits in Fig. 5.

AMTD
6, 9397–9465, 2013

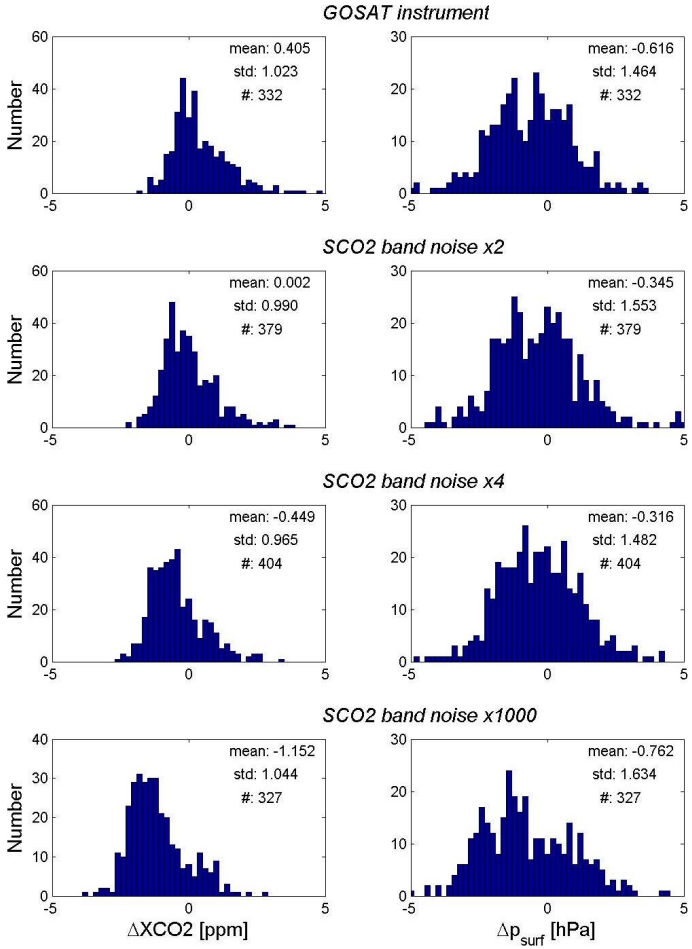

Fig. 8. Histograms of the errors in retrieved X_{CO_2} and surface pressure for different scaling factors of the noise in the strong CO_2 band.

AMTD
6, 9397–9465, 2013

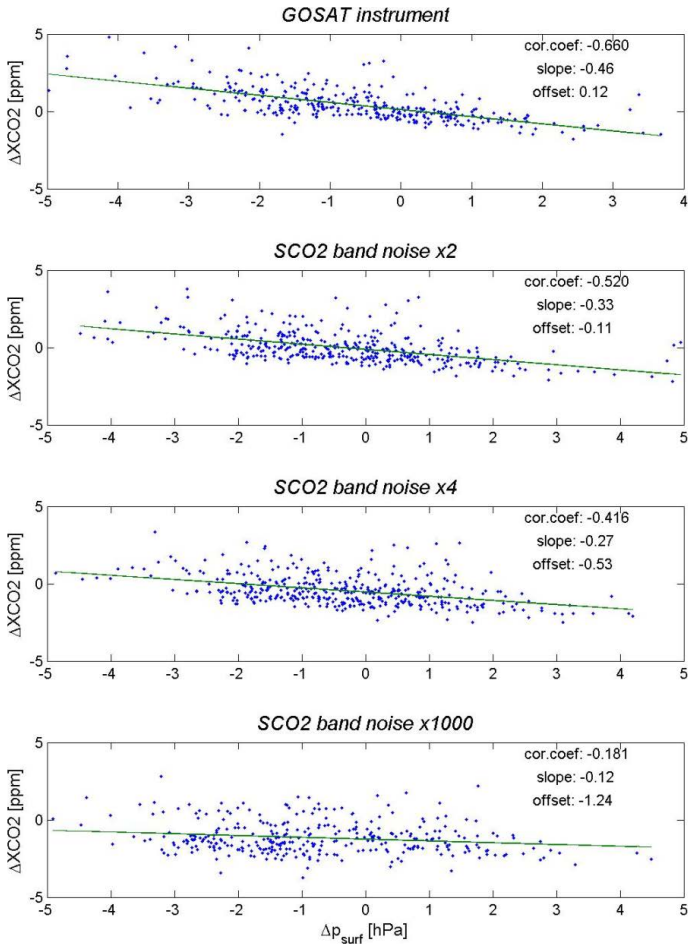

Fig. 9. Correlations between the X_{CO_2} bias and the surface pressure bias for different scaling factors of the noise in the strong CO_2 band.

AMTD
6, 9397–9465, 2013

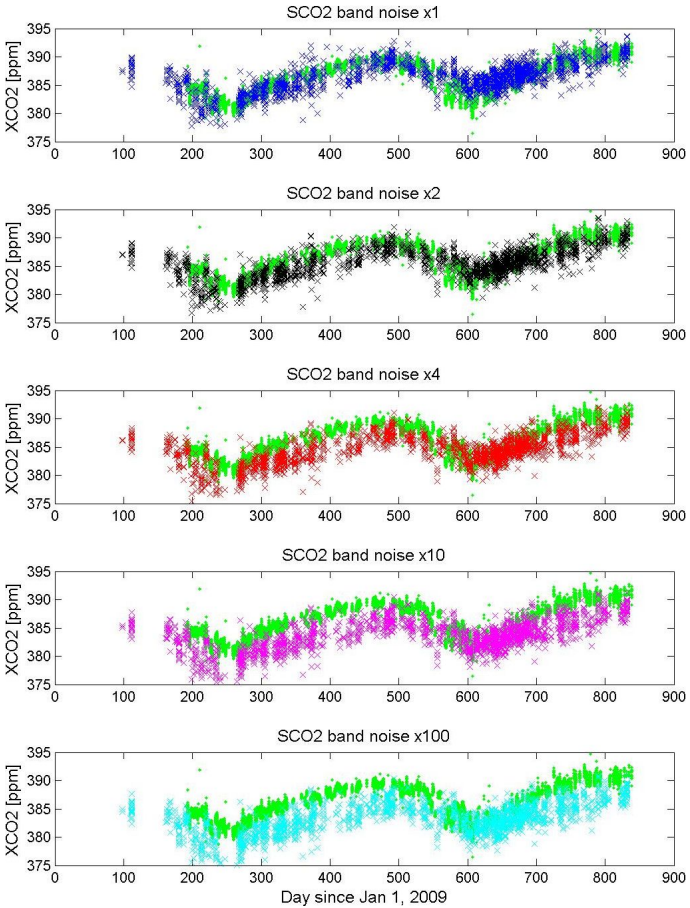

Fig. 10. Annual cycles in X_{CO_2} from TCCON and GOSAT, the latter with increasing noise in the strong CO_2 band.

AMTD
6, 9397–9465, 2013

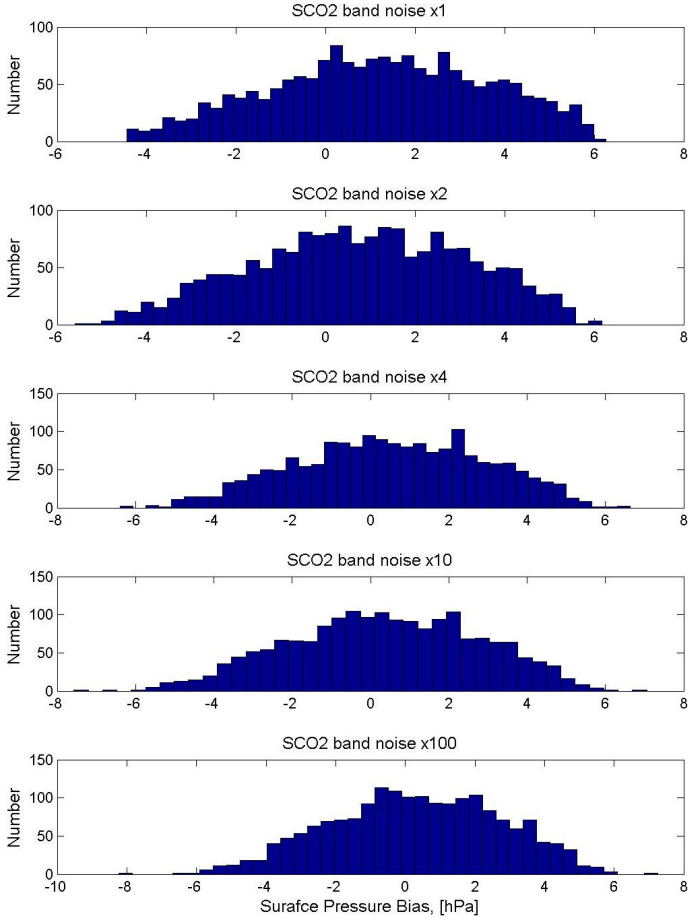

Fig. 11. Histograms of the error in retrieved surface pressure as a function of the amplification of the noise in the strong CO_2 band.

AMTD
6, 9397–9465, 2013

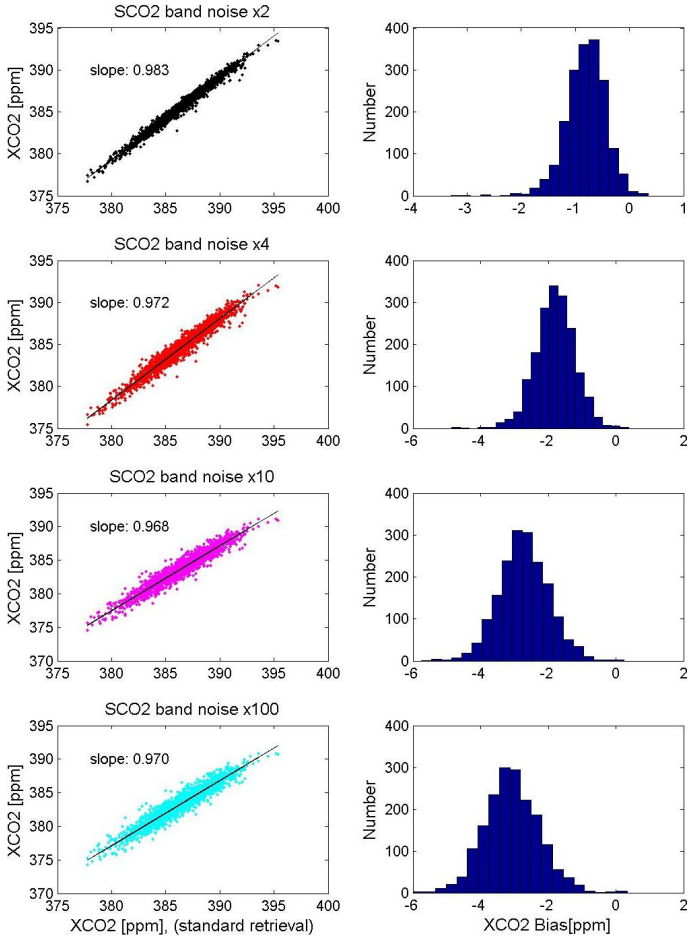

Fig. 12. Histograms of the error in retrieved X_{CO_2} as a function of the amplification of the noise in the strong CO_2 band.

AMTD
6, 9397–9465, 2013

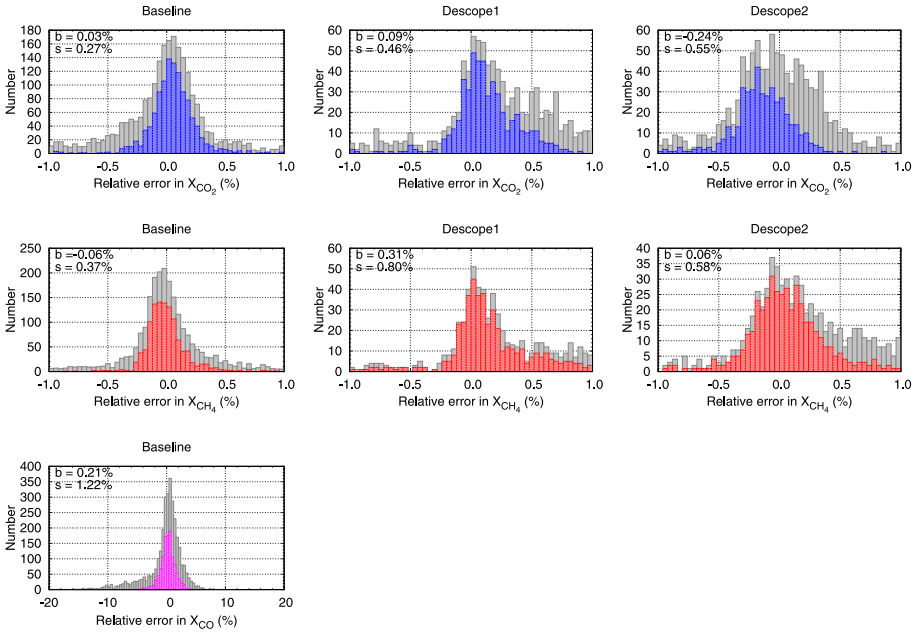

Fig. 13. Histograms of errors in retrieved X_{CO_2}, X_{CH_4} and X_{CO} for the baseline and descope configurations when the priors assumed for both the vertical profiles of CO_2, CH_4, CO and meteorology coincide with the truth. The biases (*b*) and standard deviations (*s*) quoted are for the histograms after the post-processing filters have been applied.

AMTD
6, 9397–9465, 2013

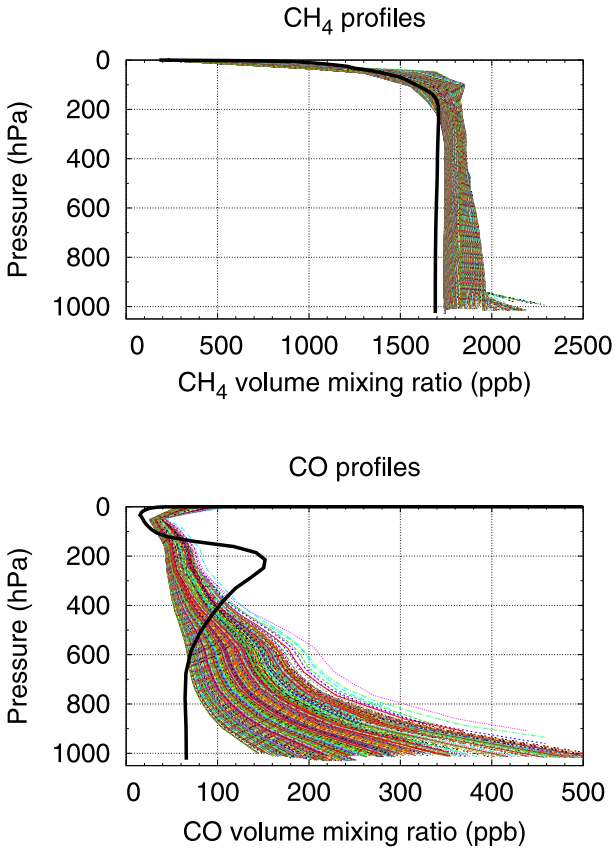

Fig. 14. The heavy black lines show the prior profiles of CH_4 and CO_2. Both are derived from simulations with the MOZART chemical transport model, and both are described as "transport" scenarios. The fine coloured lines show the true profiles for one orbit (number 4) of the simulations.

AMTD
6, 9397–9465, 2013

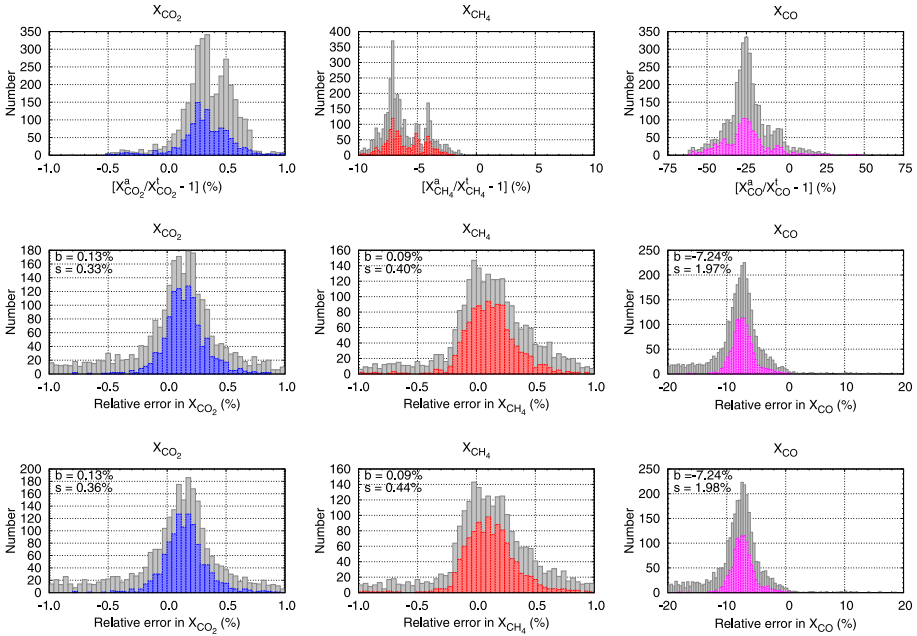

Fig. 15. The upper row compares the prior and true column amounts for the ensemble of scenes, both before and after the PPF. The lower rows present histograms of errors in retrieved X_{CO_2}, X_{CH_4} and X_{CO} for the baseline configuration when the prior profiles are approximate, as described in the text. In the middle row the priors for the meteorology coincide with the truth (experiment 2), while in the bottom row the meteorology priors also are approximate (experiment 3). The biases (b) and standard deviations (s) quoted are for the histograms after the post-processing filters have been applied.

AMTD
6, 9397–9465, 2013

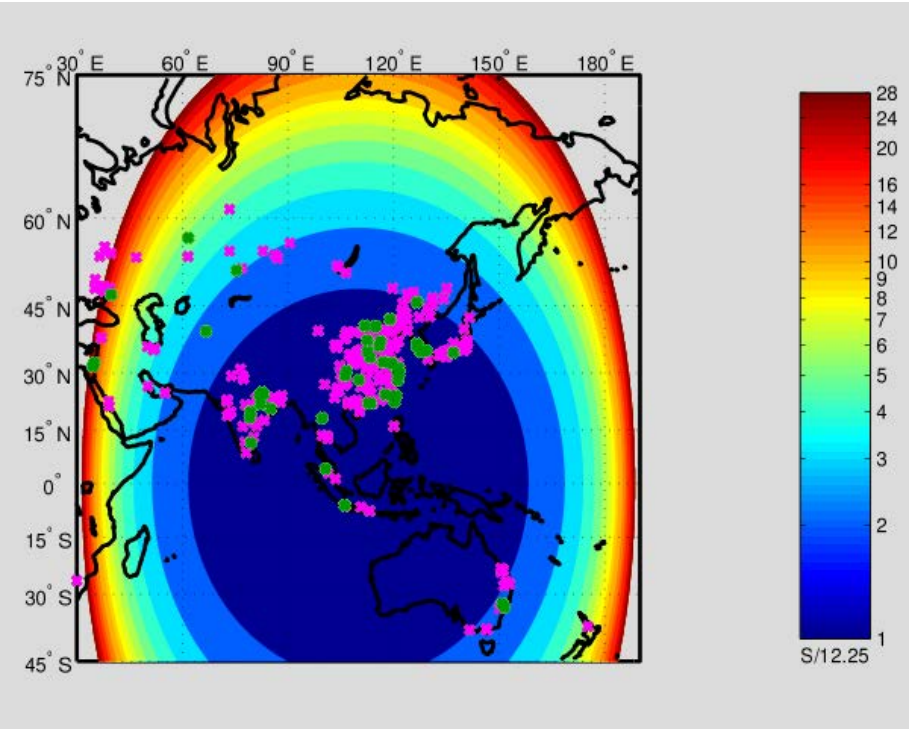

Fig. 16. Locations of power plants emitting in the range 5–15 Mt CO_2 yr^{-1} (magenta) and greater than 15 Mt CO_2 yr^{-1} (green). The backround colour shows the ratio of the geoCARB pixel area to the subsatellite pixel area (12.25 km^2).

AMTD
6, 9397–9465, 2013

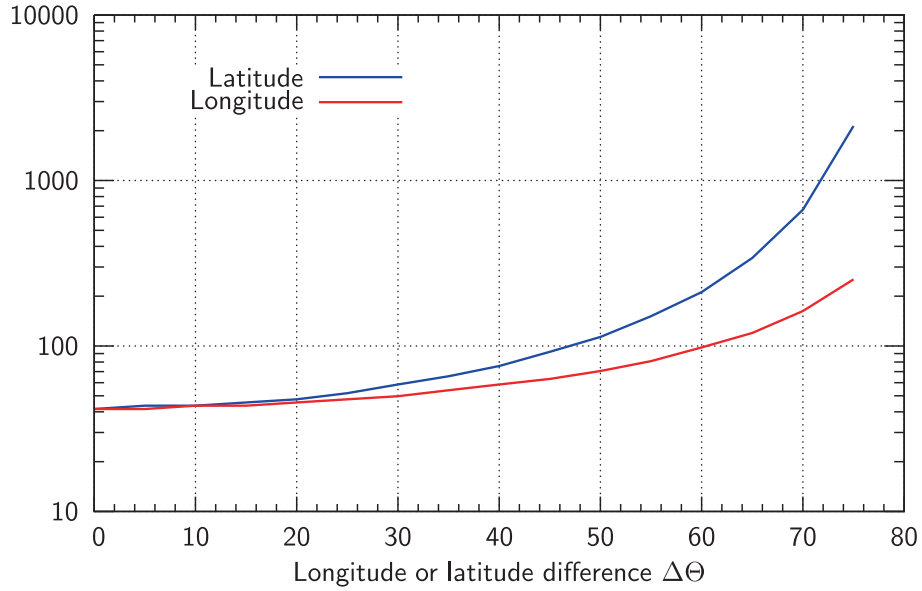

Fig. 17. Number of images of a power plant plume required to reduce the error in the estimated rate of CO_2 emission to 1 Mt CO_2 yr^{-1} as a function of difference in latitude (blue) or longitude (red), assuming that the wind blows from the west with speed 5 m s^{-1} and the standard error in estimates of X_{CO_2} is 3 ppm.

AMTD
6, 9397–9465, 2013

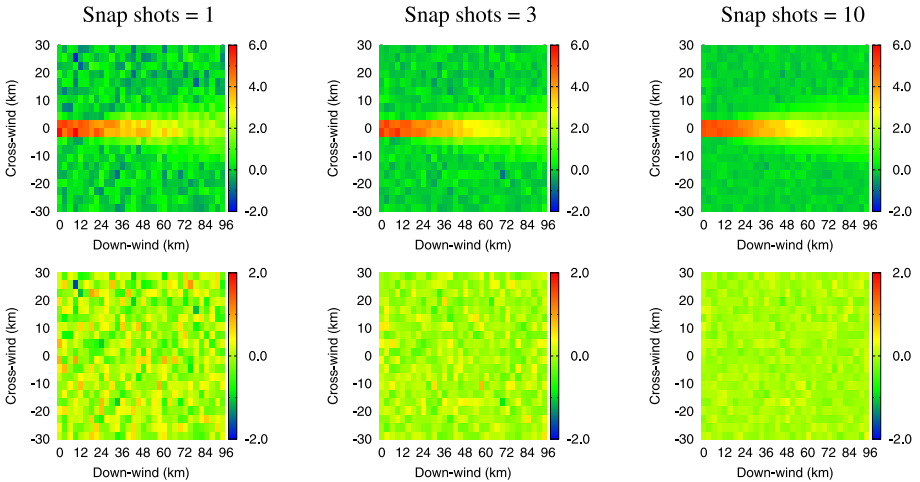

Fig. 18. The upper row shows the retrieved enhancements (in ppm) of X_{CO_2} above the background estimated from one, three and ten snap-shots. The lower row shows the corresponding errors (in ppm). The plume from the power plant is assumed to be clean (devoid of aerosol). The x- and y-axes are distances in km. The power plant is located at (0, 0). The wind is from the west with speed 1 m s^{-1}.

AMTD
6, 9397–9465, 2013
geoCARB
I. N. Polonsky et al.

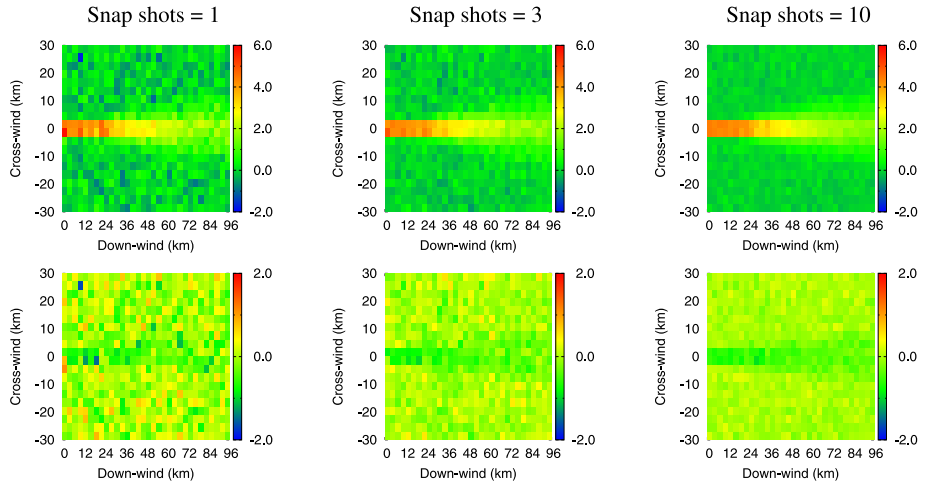

Fig. 19. As for Fig. 18 except that the plume is assumed to contain aerosol with optical thickness proportional to the X_{CO_2} enhancement. At the maximum CO_2 enhancement, the extra optical thickness of aerosol is 0.15 at the blue end of the O_2 A-band.

AMTD
6, 9397–9465, 2013

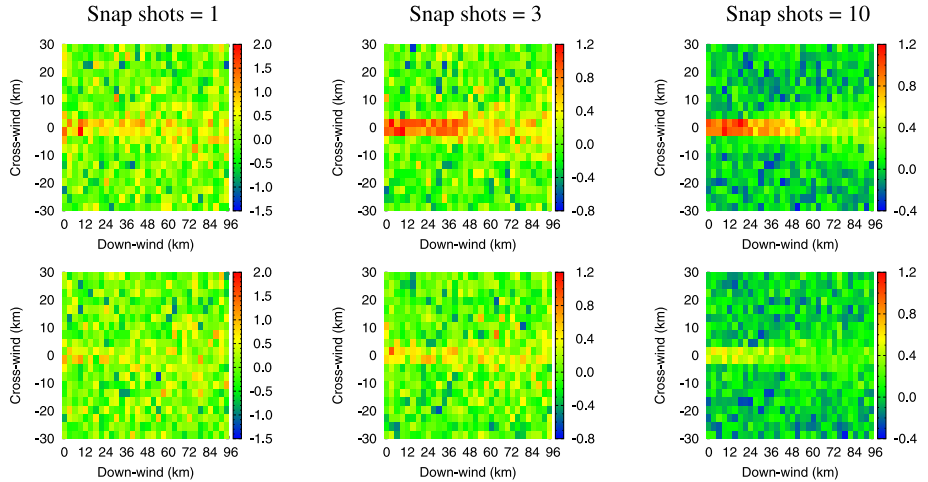

Fig. 20. The upper and lower rows show the retrieved enhancement (in ppm) of X_{CO_2} above the background estimated from one, three and ten snap-shots when the wind is from the west with speeds of $5\,m\,s^{-1}$ and $10\,m\,s^{-1}$. The plume from the power plant is assumed to be clean (devoid of aerosol). The x- and y-axes are distances in km. The power plant is located at (0, 0). Note the different colour bar ranges.

AMTD
6, 9397–9465, 2013

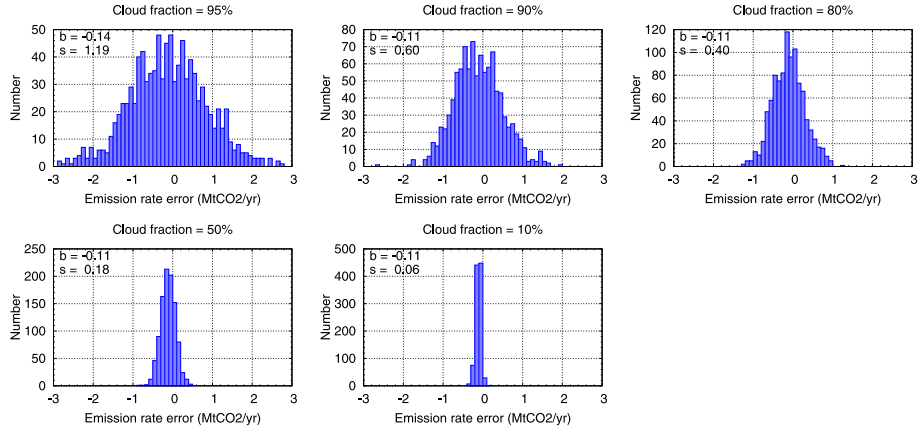

Fig. 21. Histograms of the error in retrieved emission rate (in $Mt\,CO_2\,yr^{-1}$) from 1001 simulations in which pixels are masked from the snap-shots of the power plant and its surroundings. The masking is intended to simulate situations with partial cloud cover. The panels correspond to situations with 95 %, 90 %, 80 %, 50 % and 10 % cloud cover.

AMTD
6, 9397–9465, 2013

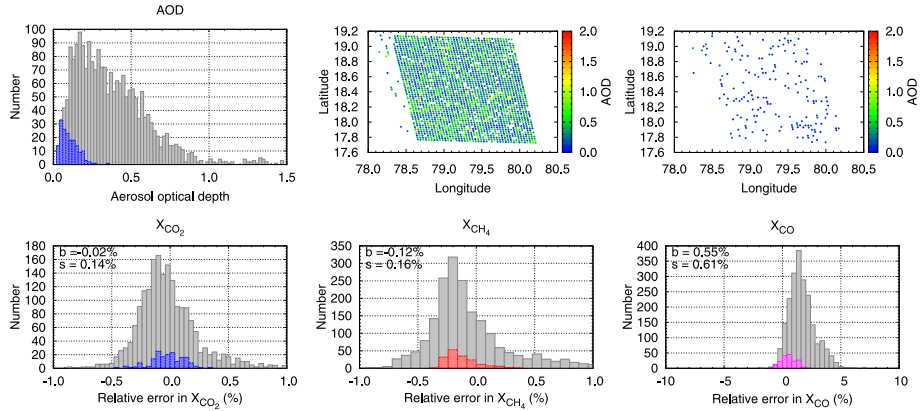

Fig. 22. The panels of the upper row show the histogram of aerosol optical depth and its spatial distribution. The points in the middle panel show the pixels where the retrieval algorithm converged, while those in the right-hand panel also passed the post-processing filter. The panels in the lower row show the histograms of errors in retrieved X_{CO_2}, X_{CH_4} and X_{CO}, again before and after the post-processing filter.

AMTD
6, 9397–9465, 2013